The State Scientific Center of Russia
The Budker Institute of Nuclear Physics
SB RAS

B.M. Fomel, M.A. Tiunov, V.P. Yakovlev

SAM – AN INTERACTIVE CODE FOR EVALUATION OF ELECTRON GUNS

Budker INP 96-11

НОВОСИБИРСК

SAM — an Interactive Code for Evaluation of Electron Guns[1]

B.M. Fomel, M.A Tiunov, V.P. Yakovlev

The State Scientific Center
Budker Institute of Nuclear Physics
630090, Novosibirsk, Russia
E-mail: tiunov@inp.nsk.su

Abstract

In 1985–86 by the authors was developed the package of computer codes SAM for evaluation of the wide range of $2D$ electromagnetostatic problems arising at designing of the injection units of accelerators and high power RF sources. Among them there are electric field calculation in the electrode systems with dielectric, magnetic field calculation in the magnetic focusing systems or systems providing the accompanying magnetic field with ferromagnetic elements (without considering the saturation effects), calculation of the ion and electron guns.

This work describes in detail the methods and algorithms used or designed by the authors at developing the package of computer codes SAM. The examples of the real electron-optics systems simulation are presented.

[1] Translation of the preprint INP 89–159

1 Introduction

One of the main trends in the development of accelerating devices is the production of linear accelerators with high accelerating rate (up to $50 \div 100\ MeV/m$). The development of RF power sources at a power of $100 \div 300\ MW$ within a wave range of $3 \div 10\ cm$ is required to achieve that accelerating rate in resonant accelerating structures. An important unit of that sources is the injector forming the high-power electron beam ($\sim 1\ MeV$) with low transverse size and phase volume with the current density of $1000\ A/cm^2$. It is known that the cathode emission current density is limited by the emission ability of present cathodes and does not exceed $10 \div 20\ A/cm^2$. Thus the required current density can be achieved only as a result of the strong compression of initial beam.

This brings up a problem of design and computer simulation of the electron-optical systems forming axial-symmetrical high-power electron beam with high compression and low phase volume. However, existing computer codes [1, 2] do not provide the accuracy needed at simulations of the high power RF sources units. Thereto these programs are realized on Large computers and work in batch regime, that very hinders the data input and processing of results.

The presented work describes the package of computer codes SAM for evaluation of electron guns of the injection units of accelerators and high

power RF sources. At its development the task to satisfy to following requirements was delivered:

1) interactive operating mode with use of computer graphics;

2) realization of codes on personal computers (IBM PC);

3) extensive care about achievement of necessary accuracy of the calculations;

4) expansion of the class of evaluating problems, including:

a) calculation of electrical fields in the electrode systems with dielectrics;

b) calculation of magnetic systems with ferromagnetics (without considering effects of saturation);

c) calculation of guns with high beam area convergence.

Though the existing codes do not satisfy to all mentioned requirements, some of them use rather of effective numerical methods and algorithms. So, in the code by V.T. Astrelin and V.Ya. Ivanov [1] the boundary elements equations method in common with spline-interpolation of surface charge density is applied. The main advantage of such approach is the a small volume of required memory at a high accuracy of calculation.

In presented work the positive experience of work of these authors was used as well as the new methods and algorithms for increasing the calculation accuracy are advanced. However, for the sake of convenience of perception, we describe all the used methods and algorithms of calculation, though some of them are already described in the works [1, 3].

At an electron guns simulation the electric and magnetic fields are presented in kind of superposition of external fields, created by electrode systems with dielectrics and with magnetic focusing elements, and own fields of beam. Thus, calculation of the gun is reduced to the consecutive solving of the two following problems:

1) electromagnetostatic;

2) calculation of the beam dynamics.

The electromagnetostatic problem is worked out by method of boundary elements equations relative to the secondary surface electric and magnetic charge density. At a numerical simulation of these equations the method of collocation with the spline-interpolation of the surface charge density is used. As a result, the initial integral equations are reduced to the two systems

of linear equations relative to the charge density in the collocation nodes. The matrix coefficients of these systems are expressed through the integrals above the electrodes surfaces and along the boundaries between dielectrics and magnetics of the product of weight spline functions into the kernel of the corresponding integral equation. These integrals are calculated numerically, and the kernel singularities of the integral equations in the collocation nodes are separated analytically to increase the accuracy of the calculations.

The accuracy of spline-interpolation sharply drops if there are singularities of fields, and as the result, singularities of the surface charge density on the sharp electrodes, dielectrics and magnetics edges, as well as in the joint points of the electrodes with the dielectrics. In this case the charge density is presented as a product of the factor, describing the singularity, into the smooth function that is good described by the spline. The initial systems of linear equations are rewritten concerning to the smooth function values in the collocation nodes, and the singularity powers are introduced under the integrals mentioned above. Thus the accuracy of calculations is increased at a sacrifice in the analytical separation of the singularities of the charge density on the edges and in the joint points, as well as the kernel singularities in the collocation nodes.

For the description of the beam dynamics in the gun the hydrodynamics current pipes model is used. The space charge and beam current distribution are described using a mesh with rectangular cells in the cylindrical coordinates (r, z) covering only the expected area of the beam particles motion. The charge and current density is considered constant within the limits of the one cell of the mesh. The electric and magnetic fields are calculated only in the mesh nodes, and evaluated in the arbitrary point with interpolation. For the description of the cathode emission the model of flat or spherical diode in dependence on the emitter form is used. To evaluate all the electron gun as a whole the method of iterations is carried out.

Especially we note the following new methods and algorithms, offered in the given work for the accuracy of calculations increasing and expansion of the class of soluble problems.

At the calculation of the electromagnetic problems:

1. Description of the charge density singularities on the dielectrics and magnetics edges, where the integral equation and its kernel lose their meaning;

2. Finding by the Mexiner method [4] of the singularity power of the

electric field close to the joint points of metals with dielectrics;

3. The low scattered magnetic fields calculation accuracy increasing through the regularization of the initial integral equation in accordance with Tozoni [5].

At the calculation of the beam dynamics:

1. The set of rectangular meshes with different sizes and subdivision of the cells, that allows to describe the charge and current non-uniform, as well as the non-uniform strong external fields more accurately. For example, non-uniform charge density in the cathode vicinity at the high beam compression or the electric field close to the anode gun aperture.

2. The parabolic interpolation at the calculation of fields in points that are not coincident with mesh nodes is used.

3. The initial approximation for iterations on the space charge is entered, that determined by the following three parameters:

a) the assumed beam current;

b) the effective anode–cathode gap;

c) the accelerating voltage on this gap.

It allows substantially to reduce the number of iterations, required for the achievement of given accuracy, especially at the calculation of the electron guns with a high perveance.

4. The singularities under integrals, that arise at the calculation of the potential and field, induced by the separate mesh cell charge inside or on the cell boundary are defined analytically. As a result the accuracy of the calculation of the beam induced potentials and fields increases significantly.

5. The current pipes have the finite section, which varies with the change of the beam radius. This allows to describe the highly non-laminar beams with high compression correctly with rather small number of the current pipes.

6. As a criterion of the iterations convergence on the space charge the convergence not only of the emitting from the cathode current, but also of the beam emittance at the exit of the gun is used.

7. At the calculation of the electric fields and potentials the matrixes of their values in the mesh nodes and collocation points at a unit surface and space charge density are previously calculated once and then are stored

on the hard disk. After that the real values of the fields and potentials in each iteration on the charge density are calculated by simple multiplication of these matrixes into the vectors of the surface charge density values in the collocation points and into the vector of the space charge density values in the mesh nodes. It allows to reduce the gun calculation time essentially at a high accuracy of the fields and potentials calculation.

The advantages of the interactive operating mode with the use of computer graphics imply that the user during calculation can see on the color graphic display the field map and the parameters of the beam in the gun. The map of the equipotentials and the electric field distribution on the gun axis, as well as the trajectories of particles, distribution of the current density and the phase diagram of the beam at the different stages of motion are thus outputted.

More the total description of the used methods and algorithms is given in the sections 2–4. In the last section the tests calculations as well as some examples of the real electron guns simulations and the comparison with the experimental results are presented.

2 Setting up a problem

At calculation of the stationary election-optical systems for the intensive beams of charged particles forming there are considered given (Fig.1):

1) the geometry and potentials of the electrodes;

2) the geometry and dielectric constant of the dielectrics;

3) the geometry and magnetic constant of the magnetic cores, as well as the geometry and currents of the coils of the magnetic focusing system;

4) the regime of the cathode emission.

The problem of simulation is to evaluate the beam formed by the given gun in terms of its own electric and magnetic (for the relativistic electron beams) fields.

To describe the space charge flux it is necessary to resolve two main equation systems simultaneously: the equation of the electromagnetic field and the beam particles motion equations.

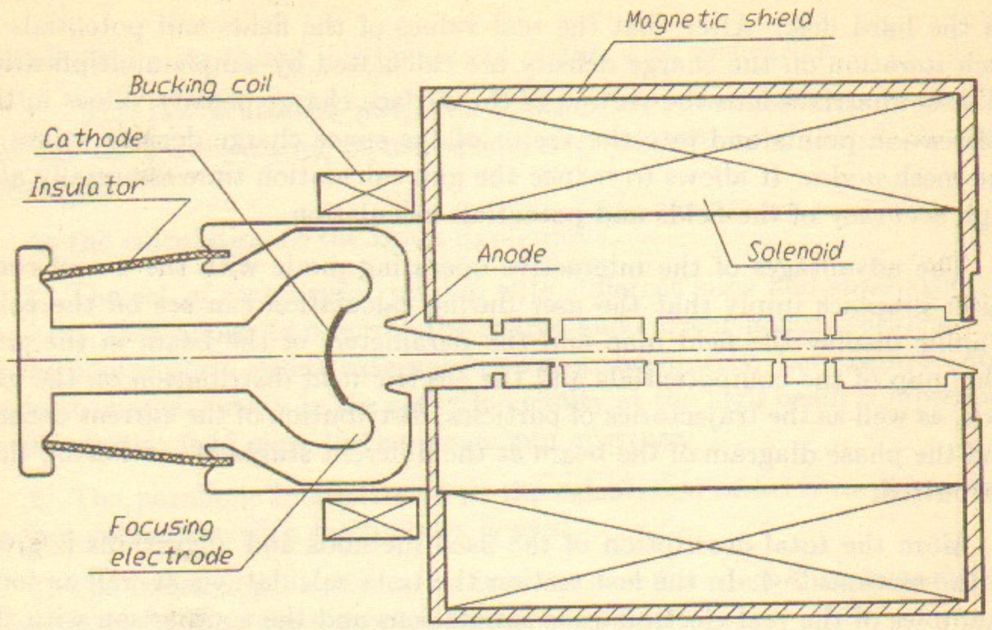

Figure 1: General view of the electron-optics system.

2.1 Equations of the electromagnetic field

By virtue of stationarity the total electric field (i.e. the field of the electrodes plus the own beam field) can be described by scalar electric potential, satisfying to the Poisson equation:

$$\Delta\varphi = -4\pi\rho\,, \tag{2.1.1}$$

where ρ — the volume charge density of the beam. On the electrodes surfaces and on the boundaries between the dielectrics with the different dielectric constants the following boundary conditions are imposed:

$$\varphi\big|_{S_e} = U_e\,, \tag{2.1.2}$$

$$\varepsilon_1\left(\frac{\partial\varphi}{\partial n}\right)_1 = \varepsilon_2\left(\frac{\partial\varphi}{\partial n}\right)_2\Bigg|_{S_d}\,, \tag{2.1.3}$$

where S_e and S_d — the surfaces of the electrodes and boundaries between the dielectrics; U_e — the potentials of the electrodes; $\frac{\partial}{\partial n}$ — the derivative

with respect to the normal to the boundary. The indexes 1 and 2 correspond to the two different mediums contiguous to the given boundary.

It is known, that the general solution of the equation (2.1.1) can be shown up as:

$$\varphi(\vec{r}_0) = \int\limits_{S_e+S_d}\frac{\sigma(\vec{r})dS}{|\vec{r}_0-\vec{r}|} + \int\limits_{V_b}\frac{\rho(\vec{r})dV}{|\vec{r}_0-\vec{r}|}\,, \tag{2.1.4}$$

where σ — the surface charge density on the electrodes and boundaries between the dielectrics; V_b — the volume, occupied by the beam. Substituting the general solution (2.1.4) into the boundary conditions (2.1.2) and (2.1.3), one can obtain the following boundary integral equations for the unknown surface charge density on the electrodes:

$$\int\limits_{S_e+S_d}\frac{\sigma(\vec{r})dS}{|\vec{r}_e-\vec{r}|} = U_e - \int\limits_{V_b}\frac{\rho(\vec{r})dV}{|\vec{r}_e-\vec{r}|} \tag{2.1.5}$$

and on the boundaries between the dielectrics:

$$2\pi\frac{\varepsilon_2+\varepsilon_1}{\varepsilon_2-\varepsilon_1}\sigma(\vec{r}_d) - \int\limits_{S_e+S_d}\sigma(\vec{r})\frac{\partial}{\partial n_d}\left(\frac{1}{|\vec{r}_d-\vec{r}|}\right)dS = \int\limits_{V_b}\rho(\vec{r})\frac{\partial}{\partial n_d}\left(\frac{1}{|\vec{r}_d-\vec{r}|}\right)dV\,, \tag{2.1.6}$$

where $\vec{r_e}$, $\vec{r_d}$ — the coordinates of points on the electrodes surfaces and demarcation boundaries respectively; $\frac{\partial}{\partial n_d}$ – derivative with respect to the normal to the boundary in the point with coordinate $\vec{r_d}$.

The own magnetic field of the beam is defined from the law of total current:

$$\oint\limits_L(\vec{B}\cdot d\vec{l}) = \frac{4\pi}{c}\int\limits_S(\vec{j}\cdot d\vec{S})\,. \tag{2.1.7}$$

Here $\vec{j}(\vec{r})$ — the beam current density, the surface S bears up against the closed contour L.

At a simulation of the beam dynamics it is necessary also to take into account the external magnetic field produced by the magnetic focusing system. Frequently for its description the paraxial approximation, that provides

the goods accuracy if the beam diameter is small in comparison with the aperture of the magnetic focusing system, is used. However, the quest to minimize the dimensions and power supply of the magnetic focusing system frequently leads to then infringement of this condition.

On the other hand, the majority of magnetic focusing system operates in the linear range of the magnetization curve of magnetic cores ($\mu = \text{const}$). In this case the magnetostatic problem can be easily resolved in total statement. To do this, one may represent the magnetic field formed by the magnetic focusing system as a sum of the current field $\vec{H}_c$ and field $\vec{H}_m$, that is produced by the induced magnet dipoles (magnetization field):

$$\vec{H} = \vec{H}_c + \vec{H}_m \,. \tag{2.1.8}$$

Entering the scalar magnetic potential to describe the magnetization field and taking into account the condition $\mu = \text{const}$, it is possible to reduce the problem of magnetization field calculation to the electrostatic problem about the dielectric in the given external field. The boundary integral equation for the "magnetic charge" surface density, similar to the equation (2.1.6), will look like:

$$2\pi\frac{\mu_2+\mu_1}{\mu_2-\mu_1}\sigma(\vec{r}_m) - \oint\limits_{S_m} \sigma(\vec{r})\frac{\partial}{\partial n_m}\left(\frac{1}{|\vec{r}_m-\vec{r}|}\right)dS = (\vec{n}_m\cdot\vec{H}_c(\vec{r}_m)) \,, \tag{2.1.9}$$

where $\vec{r}_m$ — the coordinate of point on the boundary between the magnetics; $\vec{n}_m$ — the normal vector to the border in this point; S_m — the total surface of the boundary between the magnetics.

The equations (2.1.4)—(2.1.9) form the complete set of the electromagnetic field equations in stationary electron-optical systems, forming high-perveance beams of charged particles. However, in these equations the beam charge and current densities remain indeterminate.

2.2 Equation of the beam particles motion

To describe the unknown charge and current density it is necessary to accept the any model of real beam charge particles motion. For description of stationary flows the most adequate is the hydrodynamic model of current pipes. In this model the real space charge flux is replaced by the finite

set of laminar flows or current pipes, each of that is characterized by the section-averaged values the charge and current density. Thus, by virtue of stationarity and laminarity, for each of fluxes the following equation between the current density through the pipe section and space charge density holds:

$$\vec{j} = \rho\vec{v} \,, \tag{2.2.1}$$

where $\vec{v}$ — the average speed of the charged particles, forming the given flux.

In the given fields the coordinates and speeds of particles can be found by the equation of motion

$$\frac{d\vec{P}}{dt} = e\left(-\vec{\nabla}\varphi + \frac{1}{c}[\vec{v}\times\vec{B}]\right) \tag{2.2.2}$$

with the initial conditions

$$\vec{r}\big|_{t=0} = \vec{r}_0 \,,\ \vec{v}\big|_{t=0} = \vec{v}_0 \,, \tag{2.2.3}$$

where $\vec{P} = m\gamma\vec{v}$ — the particle momentum; $\gamma = \left(1-\frac{v^2}{c^2}\right)^{-1/2}$ — the relativistic factor; $\vec{r}_0$ and $\vec{v}_0$ — the coordinate and velocity of the particle on the emitter.

According to the stationary condition the current of the given pipe does not depend on the time, hence it is constant along the pipe and is equal to

$$I = \int\limits_{S_p} \vec{j}_0(\vec{r}_0)d\vec{S} \,, \tag{2.2.4}$$

where $\vec{j}_0(\vec{r}_0)$ — the extracted from the emitter current density; S_p — the pipe section on the emitter. In case of the limitation of the emission by the space charge the current density can be approximated by the model of the flat or spherical diode in dependence on the emitter shape:

$$\vec{j}_0(\vec{r}_0) = \vec{j}_0\left(\vec{E}(\vec{r}_0,\delta),\delta\right) \,, \tag{2.2.5}$$

where $\vec{E}$ — the electric field strength on the small distance δ from the point $\vec{r}_0$ along the normal to the emitter.

Within the framework of current pipe model the equations (2.2.1)—(2.2.5) completely describe the space charge flux in the real electron-optical system at the given electric and magnetic fields.

2.3 The self-consistent problem solution

The Poisson equation (2.1.1) and, consequently, equations (2.1.5)—(2.1.6) are nonlinear, as far as their solution depends on the beam space charge density distribution. In turn, the charge distribution depends on the electric field configuration, i.e. on the equations (2.1.5)—(2.1.6) solution. The same situation arises and if the own beam magnetic field is taken into the account (formula (2.1.7)). To solve the arising self-consistent problem one shall use the method of iterations .

As initial approximation we take some beam charge and current density distribution model. Solved equations (2.1.5)—(2.1.7), we can find the electric and magnetic fields appropriate to them. After that, simulating the emission from the cathode and beam dynamics in known fields, it is possible to find the next charge and current density approximation etc. As a criterion of the iteration process convergence the small relative change from iteration to iteration of the beam current and emittance at the gun exit can serve.

Thus, the problem of the given gun analysis can be reduced to the consecutive solution of three independent problems:

a) linear magnetostatics ($\mu = \text{const}$);

b) electrostatics with the potentials and fields induced by the given beam taken into account;

c) simulation of the emission from the cathode and beam dynamics in the given fields.

The method of the two first problems solution is detailed stated in the next section. The simulation of the emission from the cathode and beam dynamics, as well as method of the induced by the beam fields and potentials calculation are separate considered in section 4.

3 Method of the boundary integral equations solution

3.1 Statement of the equations for the axial-symmetric problem

As far as hereinafter we shall consider only axial-symmetric guns and magnetic systems, it is convenient to write the boundary integral equations (2.1.5), (2.1.6) and (2.1.9) in cylindrical coordinate system (r, θ, z) and to integrate them over the angle. We designate through $\xi = (r_0,\ z_0)$ the coordinates of the point of observation and through $\eta = (r,\ z)$ the running coordinates. With these designations the mentioned equations take the form:

$$\int\limits_{L_e+L_d} \sigma(\eta)G(\xi,\eta)dl = U_e(\xi) - \int\limits_{S_b} \rho(\eta)G(\xi,\eta)dS,\ \xi \in L_e, \tag{3.1.1}$$

$$2\pi\frac{\varepsilon_1+\varepsilon_2}{\varepsilon_1-\varepsilon_2}\sigma(\xi) - \int\limits_{L_e+L_d} \sigma(\eta)\frac{\partial G}{\partial n_\xi}(\xi,\eta)dl = \int\limits_{S_b} \rho(\eta)\frac{\partial G}{\partial n_\xi}(\xi,\eta)dS,\ \xi \in L_d, \tag{3.1.2}$$

$$2\pi\frac{\mu_1+\mu_2}{\mu_1-\mu_2}\sigma(\xi) - \oint\limits_{L_m} \sigma(\eta)\frac{\partial G}{\partial n_\xi}(\xi,\eta)dl = (\vec{n}_\xi, \vec{H}_c(\xi)),\ \xi \in L_m, \tag{3.1.3}$$

where L_e, L_d, L_m — the contours of the electrodes, dielectrics and magnetics in plane (r, z); S_b — the section of the beam by this plane. The kernel of the integral equation (3.1.1)

$$G(\xi,\eta) = \int\limits_0^{2\pi} \frac{rd\theta}{\sqrt{r_0^2 - 2r_0r\cos\theta + r^2 + (z_0-z)^2}} = \frac{4K(k)r}{\sqrt{(r_0+r)^2+(z_0-z)^2}} \tag{3.1.4}$$

has a simple physical meaning. This is potential, created in the point of observation (r_0, z_0) by the infinitely thin charged ring(circle) of radius r with axial coordinate z and with unit linear charge density. In formula (3.1.4) $K(k)$ is a total elliptical integral of first kind from argument:

$$k = \sqrt{\frac{4r_0r}{(r_0+r)^2+(z_0-z)^2}}. \tag{3.1.5}$$

The kernel of the integral equations (3.1.2)—(3.1.3) coincides accurate to a sign with a normal to the boundary component of the electric field of that ring and looks like

$$\frac{\partial G}{\partial n_\xi}(\xi,\eta) = n_r \frac{\partial G}{\partial r_0}(\xi,\eta) + n_z \frac{\partial G}{\partial z_0}(\xi,\eta)\,, \qquad (3.1.6)$$

where n_r, n_z — projections of the normal to the boundary in the point of observation $(r_0,\ z_0)$,

$$\frac{\partial G}{\partial r_0}(\xi,\eta) = \frac{2r/r_0}{\sqrt{(r_0+r)^2+(z_0-z)^2}}\left[\frac{r^2-r_0^2+(z_0-z)^2}{(r-r_0)^2+(z_0-z)^2}E(k)-K(k)\right], \qquad (3.1.7)$$

$$\frac{\partial G}{\partial z_0}(\xi,\eta) = \frac{4r}{\sqrt{(r_0+r)^2+(z_0-z)^2}}\frac{(z-z_0)}{(r-r_0)^2+(z_0-z)^2}E(k)\,, \qquad (3.1.8)$$

$E(k)$ — the whole elliptical integral of second kind.

3.2 The collocation method with spline-interpolation of the solution

At numerical solving equations (3.1.1)—(3.1.3) are written in the finite number of points on the contours of the electrodes, dielectrics and magnetics $\xi_{ei} \in L_e,\ i=1,\dots,N_e;\ \xi_{dj} \in L_d,\ j=1,\dots,N_d;\ \xi_{mk} \in L_m,\ k=1,\dots,N_m$; (Fig.2). In these points – collocation nodes the values of surface charge density $\sigma_i = \sigma(\xi_i)$ are found. For the integrals calculation in left-hand parts of the equations (3.1.1)—(3.1.3), as in work [3], the interpolation of charge density by cubic spline is used:

$$\sigma(\eta(l)) = (M_{i-1}\psi_{1i}(l) + M_i\psi_{2i}(l))\frac{h_i^2}{6} + \left(\sigma_{i-1} - M_{i-1}\frac{h_i^2}{6}\right)\psi_{3i}(l) +$$

$$+ \left(\sigma_i - M_i\frac{h_i^2}{6}\right)\psi_{4i}(l),\ l_{i-1} \le l \le l_i,\ h = l_i - l_{i-1},\ i=2,\dots,N\,, \qquad (3.2.1)$$

where l — the parametrical length of the contour; $M_i = \frac{\partial^2\sigma}{\partial l^2}(l_i)$ — the second moments of the spline;

$$\psi_{1i}(l) = \frac{(l_i-l)^3}{h_i^3};\quad \psi_{2i}(l) = \frac{(l-l_{i-1})^3}{h_i^3}\,,$$

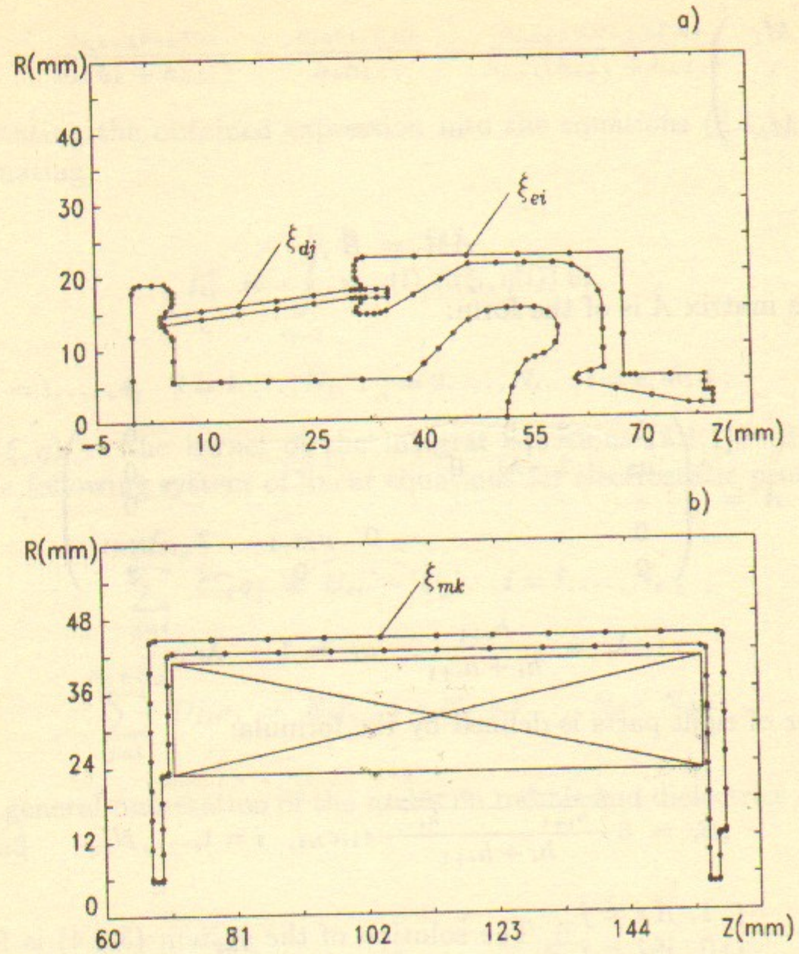

Figure 2: Arrangement of the collocation nodes on the surfaces of: a) – electrodes and dielectrics; b) – magnetics.

$$\psi_{3i}(l) = \frac{l_i-l}{h_i};\quad \psi_{4i}(l) = \frac{l-l_{i-1}}{h_i}\,, \qquad (3.2.2)$$

the weight functions of the spline. On the interpolation segment tips the additional conditions of the freely fixed tips are set:

$$M_1 = M_2,\quad M_{N-1} = M_N\,. \qquad (3.2.3)$$

From condition of continuity of the first spline (3.2.1) derivative in the collocation nodes jointly with the boundary conditions (3.2.3) we receive the following system of linear equations for the vectors of second moments

$$\vec{M} = \begin{pmatrix} M_1 \\ \vdots \\ M_N \end{pmatrix}:$$

$$\hat{A}\vec{M} = \vec{B}\,, \tag{3.2.4}$$

where the matrix $\hat{A}$ is of the form:

$$\hat{A} = \begin{pmatrix} 2 & -2 & 0 & \cdot & \cdot & \cdot & \cdot & \cdot & 0 \\ \mu_2 & 2 & \lambda_2 & 0 & \cdot & \cdot & \cdot & \cdot & 0 \\ \cdot & \cdot & \cdot & \cdot & \cdot & \cdot & \cdot & \cdot & 0 \\ 0 & \cdot & \cdot & \cdot & \cdot & 0 & \mu_{N-1} & 2 & \lambda_{N-1} \\ 0 & \cdot & \cdot & \cdot & \cdot & \cdot & 0 & -2 & 2 \end{pmatrix},$$

$$\lambda_i = \frac{h_{i+1}}{h_i + h_{i+1}}, \quad \mu_i = 1 - \lambda_i\,, \tag{3.2.5}$$

and vector of right parts is defined by the formula:

$$B_i = 6\frac{\frac{\sigma_{i+1}-\sigma_i}{h_{i+1}} - \frac{\sigma_i-\sigma_{i-1}}{h_i}}{h_i + h_{i+1}}\varepsilon_{1i}\varepsilon_{Ni}, \quad i = 1,\ldots,N\,, \tag{3.2.6}$$

where $\varepsilon_{ij} = \begin{cases} 1, & \text{if } i \neq j \\ 0, & \text{if } i = j \end{cases}$. The solution of the system (3.2.4) is found by the running method and can be written as

$$M_i = 6\sum_{k=1}^{N} a_{ik}\varepsilon_{1k}\varepsilon_{Nk}\frac{\frac{\sigma_{k+1}-\sigma_k}{h_{k+1}} - \frac{\sigma_k-\sigma_{k-1}}{h_k}}{h_k + h_{k+1}}\,, \tag{3.2.7}$$

where a_{ik} — coefficients of the matrix $\hat{A}^{-1}$. After the substitution of (3.2.7) into the formula (3.2.1) we receive

$$\sigma(l) = \sigma_{i-1}\psi_{3i}(l) + \sigma_i\psi_{4i}(l) + h_i^2\Big(\psi_{1i}(l) - \psi_{3i}(l)\Big)\sum_{k=1}^{N}\tilde{a}_{i-1,k}\sigma_k +$$

$$+ h_i^2\Big(\psi_{2i}(l) - \psi_{4i}(l)\Big)\sum_{k=1}^{N}\tilde{a}_{ik}\sigma_k\,, \quad i = 2,\ldots,N\,,$$

$$\tilde{a}_{ik} = \frac{a_{i,k-1}\varepsilon_{1k}\varepsilon_{2k}}{h_k(h_k + h_{k+1})} - \frac{a_{ik}\varepsilon_{1k}\varepsilon_{Nk}}{h_k h_{k+1}} + \frac{a_{i,k+1}\varepsilon_{N-1,k}\varepsilon_{Nk}}{h_{k+1}(h_{k+1} + h_{k+2})}\,. \tag{3.2.8}$$

Substituting the obtained expression into the equations (3.1.1)—(3.1.3) and designating

$$I_{ij}^m = \int_{l_{j-1}}^{l_j} \psi_{mj}(l)\, R(\xi_i, \eta(l))\, dl,$$

$$m = 1,\ldots,4, \quad i = 1,\ldots,N_t, \quad j = 2,\ldots,N_t, \quad t = e,m,d\,, \tag{3.2.9}$$

where $R(\xi,\eta)$ — the kernel of the integral equations (3.1.1)—(3.1.3), we obtain the following system of linear equations for electrostatic problem:

$$\sum_{j=1}^{N_e+N_d} C_{ij}\sigma_j = U_{ei} - U_{\rho i}, \quad i = 1,\ldots,N_e\,;$$

$$\sum_{j=1}^{N_e+N_d} D_{ij}\sigma_j = E_{ni}, \quad i = N_e+1,\ldots,N_e+N_d\,; \tag{3.2.10}$$

Here the general numeration of the nodes on metals and dielectrics are introduced, and

$$C_{ij} = \varepsilon_{Nn}I_{in}^3 + \varepsilon_{1n}I_{in}^4 + \sum_{k=2}^{N} h_k^2(I_{ik}^1 - I_{ik}^3)\tilde{a}_{k-1,n} + \sum_{k=2}^{N} h_k^2(I_{ik}^2 - I_{ik}^4)\tilde{a}_{kn}\,, \tag{3.2.11}$$

where $n = j$, $N = N_e$ at $j \le N_e$ and $n = j - N_e$, $N = N_d$ at $j > N_e$;

$$D_{ij} = 2\pi\frac{\varepsilon_2 + \varepsilon_1}{\varepsilon_2 - \varepsilon_1}\delta_{ij} - C_{ij}^*\,, \tag{3.2.12}$$

where C_{ij}^* is coincident with C_{ij} accurate to a kernel change in the integrals (3.2.9). In the system (3.2.10) also the following designations are introduced:

$$U_{\rho i} = \int_{S_b} \rho(\eta)G(\xi_i,\eta)dS\,,$$

$$E_{ni} = \int_{S_b} \rho(\eta)\frac{\partial G}{\partial n_{\xi_i}}(\xi_i,\eta)dS\,, \tag{3.2.13}$$

for the potential and the normal component of the electric field, induced by the beam in the collocation nodes.

For the magnetostatic problem the similar equation system will look like

$$\sum_{j=1}^{N_m} F_{ij}\sigma_j \;=\; (\vec{n}_i, \vec{H}_{ci}) \;, \quad i = 1, \ldots, N_m \;, \tag{3.2.14}$$

where the matrix F_{ij} coincides with the matrix D_{ij} (3.2.11) accurate to numbering of elements and changing from ε to μ.

Thus, the initial integral equations (3.1.1)—(3.1.3) can be reduced to the two systems of linear algebraic equations (3.2.10) and (3.2.14). Therewith the accuracy of the spline interpolation of the surface charge density in its values in nodes reaches $o(h^4)$, where $h = \max\limits_i h_i$. In turn, accuracy of calculation of the charge density in nodes depends on the accuracy of calculation of the integrals (3.2.9). Analytical expressions for these integrals do not exist, therefore they are calculated numerically by the Gauss quadratures method. However, the accuracy of numerical integration sharply drops because of the singularity of the integral equations kernel $R(\xi_i, \eta)$ in case when the point of observation coincides with the beginning or end of the interval of integration ($i = j - 1$ or $i = j$).

3.3 Separation of the integral equations kernel singularity

In case mentioned above let us do following. Let the point of observation coincides, for example, with the end of the integration segment $\xi_i = \eta(l_j)$, $i = j$. We conduct a tangent line to the contour of integration in this point and designate it $\tilde{\eta}(l)$ (Fig.3). Obviously, that in limit $l \to l_j$ the difference $R(\xi_j, \eta) - R(\xi_j, \tilde{\eta})$ tends to zero. Let expand the function $R(\xi_j, \tilde{\eta})$ into a series on a small parameter $\varepsilon = \frac{\rho}{r_j}$, where ρ — the distance between the point of observation $\xi_i = (r_j, z_j)$ and point on the tangent line $\tilde{\eta}(l)$. We designate obtained by this means the kernel asymptotics at $\tilde{\eta}(l) \to \xi_j$ in the form of $\tilde{R}(\xi_j, \tilde{\eta})$ (see the Appendix A.1). The initial integrals (3.2.9) can be submitted in following form:

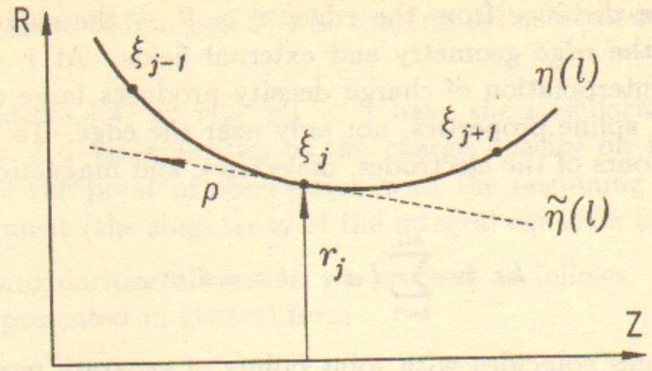

Figure 3: Tangent line to the contour of integration.

$$I_{ij}^m = \int\limits_{l_{j-1}}^{l_j} \psi_{mj}(l)\left[R(\xi_j, \eta(l)) - \tilde{R}(\xi_j, \tilde{\eta}(l))\right] dl + \int\limits_{l_{j-1}}^{l_j} \psi_{mj}(l)\tilde{R}(\xi_j, \tilde{\eta}(l)) dl \;. \tag{3.3.1}$$

In the formula (3.3.1) the first integral has not already a singularity and can be numerically calculated with a good accuracy. The remaining integral is taken analytically (see Appendix A.1).

In case when the point of observation coincides with the beginning of the integration segment the singularity is separated in a similar way. Notice that obtained by that way kernel asymptotic is not defined if the point of observation is located on the axis of the system. However, from formulas (3.1.4), (3.1.7), and (3.1.8) it is easily to see, that at $r \to r_0 = 0$ the kernel has not a singularity and integrals (3.2.9) can be calculated numerically with good accuracy.

3.4 Separation of the solution singularities

The other complexity at boundary integral equations (3.1.1)—(3.1.3) solution is that the desired surface charge density may have a singularity on the metals, dielectrics, and magnetics edges. The nature of this singularity in general case looks like [4]:

$$\sigma \sim \rho^{\tau - 1} \;, \tag{3.4.1}$$

where ρ — the distance from the edge; $\tau > 0$ — the singularity power, depending on the edge geometry and external fields. At $\tau < 1$ the cubic spline (3.2.1) interpolation of charge density produces large error, and, on the strength of spline properties, not only near the edge. To avoid this, we divide the contours of the electrodes, dielectrics, and magnetics into parts

$$L_t = \sum_{k=1}^{M_t} L_{tk}\,, \quad t = e, d, m\,, \tag{3.4.2}$$

So that the edges coincides with joint points of separate parts. Then the charge density on each of the intervals $0 \le l \le L_{tk}$ can be presented in following form:

$$\sigma(l) = \left(\frac{l}{L_{tk}}\right)^{\tau_{1k}-1} \cdot \left(\frac{L_{tk}-l}{L_{tk}}\right)^{\tau_{2k}-1} \cdot \tilde{\sigma}(l)\,, \tag{3.4.3}$$

where $\tilde{\sigma}(l)$ is a smooth function good described by the spline, and multipliers before it describe the singularity of the charge density on the edges of type (3.4.1) with powers τ_{1k} and τ_{2k} at the beginning and at the end of given part of the contour, respectively. On the each part of the contour L_{tk} we build its own spline to describe the smooth function $\tilde{\sigma}(l)$.

We emphasize that on the metal surfaces the spline nodes (points of observation) can be placed on the edges, where the equation (3.1.1) and its kernel are defined. Therefore the formulas (3.1.1)—(3.2.10) remain in force for the points, belonging to the electrodes, accurate to replacement $\sigma_i \to \tilde{\sigma}_i$ and addition of a summation over the segments L_{ek}, and integrals (3.2.9) will look like

$$I_{ij}^m = \int_{l_j-1}^{l_j} \left(\frac{l}{L_{ek}}\right)^{\tau_{1k}-1} \left(\frac{L_{ek}-l}{L_{ek}}\right)^{\tau_{2k}-1} \cdot \psi_{mj}(l) \cdot R(\xi_i, \eta(l))\, dl,$$

$$m = 1, \ldots, 4, \quad i = 1, \ldots, N_{ek}, \quad , j = 2, \ldots, N_{ek}\,. \tag{3.4.4}$$

Moreover, it is possible to write the condition of continuity for the charge density in the joint points of the separate parts of L_{ek}, for example, for k-th and $k+1$-th:

$$\tilde{\sigma}_{N_k} = \left(\frac{L_{ek}}{L_{ek+1}}\right)^{\tau-1} \cdot \tilde{\sigma}_1\,, \tag{3.4.5}$$

where $\tau = \tau_{2k} = \tau_{1,k+1}$; N_k — the number of the spline nodes on the segment L_{ek}; $\tilde{\sigma}_1$ — the value of function $\tilde{\sigma}(l)$ in the first spline node on the segment L_{ek+1}.

The integrals (3.4.4) at τ_{1k}, $\tau_{2k} < 1$ have the singularities just as at $l = 0$ and $l = L_{ek}$ (singularities of the charge density on the edges), as at alignment of the point of observation with the beginning or end of the integration segment (the singularity of the integral equation kernel).

For these singularities allocation we proceed as follows. The integrals (3.4.4) can be presented in general form

$$I_{ij}^m = \int_0^1 P_j(x)\, Q_m(x)\, R_{ij}(x)\, dx\,, \tag{3.4.6}$$

where the function $P_j(x)$ describes the singularity on the edges, i.e. at $j = 2$, $x = 0$, and $j = N_k$, $x = 1$, function $Q_m(x)$ accurate to the multiplier coincides with the weight functions of the spline, $R_{ij}(x)$ — kernel of the integral equations (3.1.1)—(3.1.3), possessing the singularities at $i = j - 1$, $x = 0$ and $i = j$, $x = 1$. At allocation of the singularities one shall recognize the following two main cases:

1. Point of observation does not coincide with ends of interval of integration. In this case in the all intervals, except for the first and the latest, the function under the integral sign has not singularity and integrals (3.4.6) are calculated numerically. The singularity of the function $P_j(x)$ on the first ($j = 2$) and the latest ($j = N_k$) intervals of integration is allocated as follows:

$$I_{ij}^m = \int_0^1 P_j(x)\,[Q_m(x)R_{ij}(x) - Q_m(a)R_{ij}(a)]\,dx + Q_m(a)R_{ij}(a)\int_0^1 P_j(x)dx\,, \tag{3.4.7}$$

where $a = 0$ at $j = 2$ and $a = 1$ at $j = N_k$. In formula (3.4.7) the first integral has not the singularity and is integrated numerically, and the second — analytically.

2. Point of observation coincides with the beginning or end of the interval of integration ($i = j - 1$ or $i = j$). If it is not the outer interval ($j \ne 2$ and $j \ne N_k$), so only the kernel R_{ij} has the singularity and the integral (3.4.6) may be written as:

$$I_{ij}^m = \int_0^1 Q_m(x)\left[P_j(x)R_{ij}(x) - P_j(a)R_{ij}(x)\right]dx + P_j(a)\int_0^1 Q_m(x)\tilde{R}_{ij}(x)dx\ , \tag{3.4.8}$$

where $\tilde{R}_{ij}(x)$ — the asymptotics of a kernel at $x \to a$, with $a = 0$ at $i = j-1$ and $a = 1$ at $i = j$. The first integral already has not the singularity, and the second one coincides with the additional integral in formula (3.3.1) and is presented in Appendix A.1.

If the point of observation coincides with the beginning of first or end of last interval of integration, i.e. is located on the electrode edge, so in this point not only the kernel of equation (3.1.1), but also its solution (functions $P_j(x)$ and $R_{ij}(x)$ in formula (3.4.6)) has a singularity. For allocation of the singularity we present the integral (3.4.6) in following form:

$$I_{ij}^m = \int_0^1 P_j(x)Q_m(x)\left[R_{ij}(x) - \tilde{R}_{ij}(x)\right]dx + \int_0^1 P_j(x)Q_m(x)\tilde{R}_{ij}(x)dx\ . \tag{3.4.9}$$

Here or $i = 1,\ j = 2$, or $i = j = N_k$; $\tilde{R}_{ij}(x)$ — asymptotics of the kernel at $x \to 0$ in the first and at $x \to 1$ in the last interval of integration.

If the point of observation coincides with the end of the first or with the beginning of the last interval, so on the one of limits of integration in (3.4.6) it is the kernel of equation (3.1.1) that has a singularity, and on another it is its solution . In that case the integral (3.4.6) can be presented in the following form:

$$I_{ij}^m = \int_0^1 \{P_j(x)\left[Q_m(x)R_{ij}(x) - Q_m(a)R_{ij}(a)\right] - P_j(1-a)Q_m(1-a)\tilde{R}_{ij}(x)\}dx +$$

$$+Q_m(a)R_{ij}(a)\int_0^1 P_j(x)dx + P_j(1-a)Q_m(1-a)\int_0^1 \tilde{R}_{ij}(x)dx\ , \tag{3.4.10}$$

where $a = 0$ at $i = j = 2$ and $a = 1$ at $i = j-1,\ j = N_k$; $\tilde{R}_{ij}(x)$ — the kernel asymptotics at $x \to 1-a$. The expression in curly braces in formula (3.4.10)

already has not singularities, and other integrals are calculated analytically. Formulas (3.4.6)—(3:4.10) are adduced more detailed in Appendix A.2.

The question about the allocation of singularities on the edges of dielectrics and magnetics, as well as in the joint points between a metal and dielectric and between various dielectrics or magnetics with one another, demands the individual consideration. The fact is that in these points the direction of a normal is not defined, so and the kernel of equations (3.1.2)—(3.1.3). Besides the charge density in these points can tend to the infinity and then equations , (3.1.2)—(3.1.3) unlike the equation (3.1.1), simply lose their meaning.

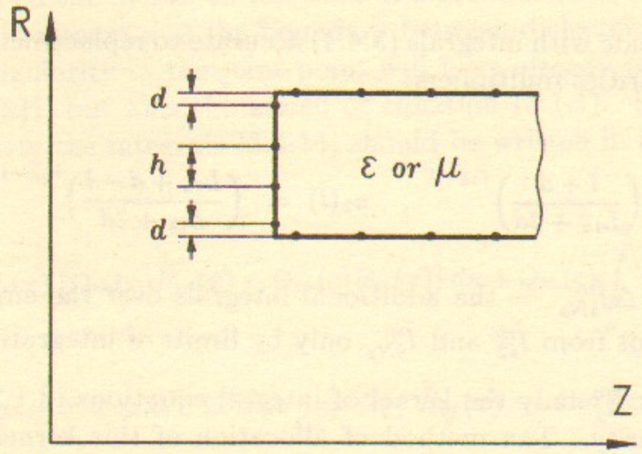

Figure 4: Arrangement of the collocation nodes close to the dielectric (magnetic) edges.

The presented work offers the following method of allocation of singularities on the edges of dielectrics and magnetics, as well as in the joint points of various materials. We consider the part of the boundary between dielectrics or magnetics, for example, abutting on the corner (see Fig.4). We remove from the corner the outer point of observation on this boundary on some small finite distance $d \ll h$, where h — the step of spline, describing the charge density on this boundary.

At the same time in integrals in left-hand parts of equations (3.1.1)—(3.1.3) the contribution from the small segment d shall be taken into account. It can be significant owing to the singularity of the charge density in the corner. To describe the charge density on the segment d the extrapolations with the spline, constructed on the given part of the boundary between dielectrics

or magnetics, will be used. Similarly we proceed on the other end of the considered part of the boundary, which also can adjoin to the corner or to the joint point of different materials.

It will be considered, that spline is still built on interval $0 \le l \le L_{tk}$. In view of two small segments d on the boundaries, the total length of the given part of the boundary will be equal to $L_{tk} + 2d$, and parameter l will vary in limits $-d \le l \le L_{tk} + d$. Then on the boundary between dielectrics or magnetics the integrals (3.4.4) can be submitted in following form:

$$I_{ij}^m = \tilde{I}_{ij}^m + \delta_{2j}\Delta\tilde{I}_{i2}^m + \delta_{N_k j}\Delta\tilde{I}_{iN_k}^m , \qquad (3.4.11)$$

where $\tilde{I}_{ij}^m$ coincide with integrals (3.4.4) accurate to replacement of the charge density singularities multipliers:

$$a_1(l) = \left(\frac{l+d}{L_{tk}+2d}\right)^{\tau_{1k}-1} , \quad a_2(l) = \left(\frac{L_{tk}+d-l}{L_{tk}+2d}\right)^{\tau_{2k}-1} , \qquad (3.4.12)$$

and $\Delta\tilde{I}_{i2}^m$ and $\Delta\tilde{I}_{iN_k}^m$ — the additional integrals over the small segments d and are different from $\tilde{I}_{i2}^m$ and $\tilde{I}_{iN_k}^m$ only by limits of integration.

In integrals $\tilde{I}_{ij}^m$ only the kernel of integral equations (3.1.2)—(3.1.3) can have a singularity. The method of allocation of this kernel singularity is similar to the method of the kernel singularity allocation on the metal surfaces in formula (3.4.8).

The integrals $\Delta\tilde{I}_{i2}^m$ and $\Delta\tilde{I}_{iN_k}^m$ can be written in following general form:

$$\Delta\tilde{I}_{ij}^m = \int_a^b P_j(x)\, Q_m(x)\, R_{ij}(x)\, dx , \qquad (3.4.13)$$

that is completely similar to formula (3.4.6), except that here or $j = 2$ and then $a = -\delta$, $b = 0$, or $j = N_k$ and $a = 1$, $b = 1 + \delta$, where $\delta = d/h \ll 1$. Notice also, that function $P_j(x)$ that is equal to the product of multipliers (3.4.12), in the both integrals has a singularity or at $j = 2$ and $x = -\delta$, or at $j = N_k$ and $x = 1 + \delta$ (a singularity of the solution). If the point of observation does not belong to the interval of integration, the singularity of function $P_j(x)$ is allocated by following way (see formula (3.4.7)):

$$\Delta\tilde{I}_{ij}^m = \int_a^b P_j(x)\,[Q_m(x)R_{ij}(x) - Q_m(c)R_{ij}(c)]\,dx + Q_m(c)R_{ij}(c)\int_a^b P_j(x)dx , \qquad (3.4.14)$$

where $c = a$ at $j = 2$ and $c = b$ at $j = N_k$.

The following two cases require the individual consideration:

1) point of observation coincides with the joint point of metal with the boundary between dielectrics. It is possible only in the case when the point of observation is on the metal. In this case at a calculation of integrals (3.4.13) over the small segment d of the boundary between dielectrics, contiguous to the metal, singularity in the joint point will have already not only solution (function $P_j(x)$), but also the kernel of equation (3.1.1). For allocation of these singularity the integrals (3.4.13) should be written in following form:

$$\Delta\tilde{I}_{ij}^m = \int_a^b P_j(x)\left[Q_m(x)R_{ij}(x) - Q_m(c)\tilde{R}_{ij}(x)\right]dx + Q_m(c)\int_a^b P_j(x)\tilde{R}_{ij}(x)dx , \qquad (3.4.15)$$

where $c = a$ at $j = 2$ and $c = b$ at $j = N_k$; $\tilde{R}_{ij}(x)$ — the kernel asymptotics at $x \to c$;

2) point of observation is an outer point on the boundary between dielectrics or magnetics. In this case in integrals (3.4.13) the kernel of equations (3.1.2)—(3.1.3) will have a singularity on the other limit in comparison with the previous case. For allocation of the singularity of the solution and kernel the integral (3.4.13) should be presented in form, similar to the formula (3.4.10):

$$\Delta\tilde{I}_{ij}^m = \int_a^b \{P_j(x)\,[Q_m(x)R_{ij}(x) - Q_m(c)R_{ij}(c)] - P_j(f)Q_m(f)\tilde{R}_{ij}(x)\}dx +$$

$$+Q_m(c)R_{ij}(c)\int_a^b P_j(x)dx + P_j(f)Q_m(f)\int_a^b \tilde{R}_{ij}(x)dx , \qquad (3.4.16)$$

where $c = a$ and $f = b$ at $j = 2$, and $c = b$ and $f = a$ at $j = N_k$; $\tilde{R}_{ij}(x)$ — the kernel asymptotics at $x \to f$. It is clear that in this representation the

expression in curly braces has not a singularity, and two remaining integrals are calculated analytically.

Formulas (3.4.13)—(3.4.16) are adduced more detailed in Appendix A.2.

3.5 Finding of the field singularity parameter

The accuracy, achievable by allocation of a singularity of the charge density, depends mostly on the accuracy of definition of the parameter of field singularity on the sharp edges of electrodes, dielectrics and magnetics, as well as in the joint points. The behaviour of field in close proximity to the edge or joint point on distances, small in comparison with distance from this point to axis of system will be searched. Then the problem of finding of singularity parameter can be considered in plane approximation. The exception is the case when the field has a singularity on the axis of system (for example, conic point).

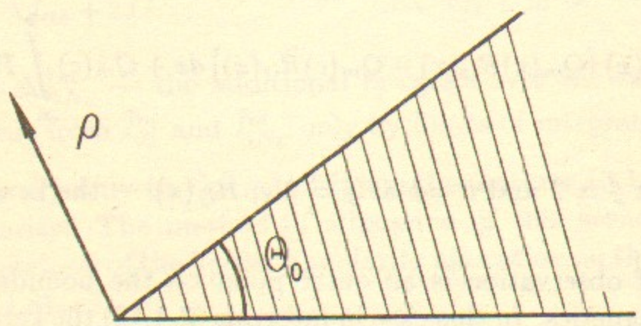

Figure 5: Metal wedge with the wedge angle Θ_0.

It is known, that the analytical solution about behaviour of the field in the vicinity of the flat wedge-like edge of the conductor [7] (see Fig.5) exists:

$$E \sim \rho^{\tau-1}, \quad \tau = \frac{\pi}{2\pi - \theta_0}, \tag{3.5.1}$$

where ρ — the distance from the edge, θ_0 — the wedge angle. The solution can be used for description of the singularity of the magnetic field in the vicinity of sharp magnetic edge with the constraint $\mu \gg 1$. The problem of finding the field singularity parameter in the vicinity of dielectric wedge or joint point of some dielectric media one with other and with the metals require the individual consideration. To do this the advantages of well-known

Mexiner method [4] will be taken with applying it to the static field description [8].

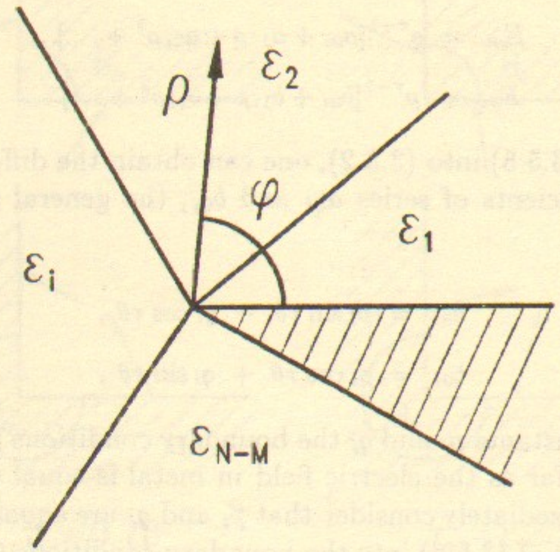

Figure 6: Joint point of several dielectric media and metals.

Let we have the joint point of N media with the different dielectric constants ε_i, among which are $M < N$ metals. Introduce the polar coordinates system $(\rho,\ \theta)$, the center of which coincides with the joint point (see Fig.6). The electric field should satisfy to the electrostatics equations:

$$\begin{aligned} \mathrm{div}\vec{D} &= 0\,, \\ \mathrm{rot}\vec{E} &= 0 \end{aligned} \tag{3.5.2}$$

and to the boundary conditions:

a) on the boundary between the dielectrics

$$\begin{aligned} \varepsilon_i E_{\theta i} &= \varepsilon_{i+1} E_{\theta i+1}\,, \\ E_{\rho i} &= E_{\rho i+1}\,; \end{aligned} \tag{3.5.3}$$

b) on the conductors surface

$$E_{\rho i} = E_{\rho i+1} = 0\,. \tag{3.5.4}$$

The solution of the equations (3.5.2) will be searched in the form of the asymptotic series:

$$E_{\rho i} = \rho^{\tau-1}[a_{0i} + a_{1i}\rho + a_{2i}\rho^2 + \ldots] ,$$
$$E_{\theta i} = \rho^{\tau-1}[b_{0i} + b_{1i}\rho + b_{2i}\rho^2 + \ldots] . \qquad (3.5.5)$$

Substituting (3.5.5) into (3.5.2), one can obtain the differential equations for the first coefficients of series a_{0i} and b_{0i}, the general solution of which takes the form of

$$a_{0i} = p_i \sin\tau\theta - q_i \cos\tau\theta ,$$
$$b_{0i} = p_i \cos\tau\theta + q_i \sin\tau\theta , \qquad (3.5.6)$$

To find the constants p_i and q_i the boundary conditions (3.5.3) and (3.5.4) will be used. As far as the electric field in metal is equal to zero, for metal media we can immediately consider that p_i and q_i are equal to zero. A result of the substitution of (3.5.6) into the boundary conditions (3.5.3) and (3.5.4) is the uniform system of $2 \cdot (N - M)$ equations:

$$\hat{A}(\tau) \cdot \vec{P} = 0 , \qquad (3.5.7)$$

where $\hat{A}(\tau)$ — the system matrix; $\vec{P} = \left\{ \begin{array}{c} p_i \\ q_i \end{array} \right\}$, $i = 1, \ldots, N - M$.

The system (3.5.7) has the nontrivial solution with the proviso that the determinant of matrix $\hat{A}(\tau)$ is equal to zero:

$$\det\hat{A}(\tau) = 0 . \qquad (3.5.8)$$

This condition allows to determine the singularity parameter of the electric field in the general case.

Specially notice, that in the given method of solution at $M = 0$ the information about configuration of the external fields is not available completely. Therefore, if several solutions of equation (3.5.8) exist, the question arises of choosing the physical solution, appropriate to the given distribution of the external electric field. For example, for a dielectric wedge with $\varepsilon = 5$ and a wedge angle of $\theta_0 = 90°$ one can obtain from (3.5.8) two values of singularity parameter $\tau_1 = 0.78$ and $\tau_2 = 1.22$. The same values result for a wedge with $\theta_0 = 270°$. Therewith to each value θ_0 there corresponds its own

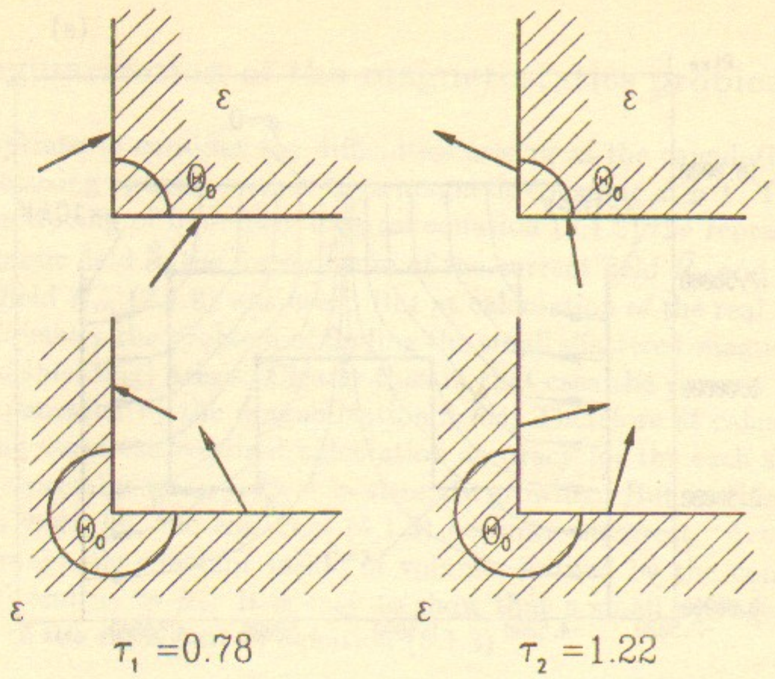

Figure 7: Character of the electric field behavior and appropriate values of the singularity power τ for the two dielectric wedges with $\varepsilon = 5$ and wedge angles of 90° and 270°.

configuration of the electric field in the vicinity of the wedge edge, that are schematically represented on Fig.7. Notice, that at $\tau < 1$ the electric field and, consequently, surface charge density have a singularity on the edge for the both values of the wedge angle.

To illustrate aforesaid we consider the dielectric cap with $\varepsilon = 5$, placed in the electric field with the special configuration (Fig.8). In this case the surface charge density has a singularity in points 3, 4 and 5 and vanishes in point 2. Below on the same drawing the distribution of the charge density on the dielectric along the polygonal line 123456 is represented.

From this simple example it is evident that in the general case it is difficult to choose the right value of singularity parameter at once. Besides the singularity allocation needs to be done and at $1 < \tau < 2$. Actually in this case the charge density as the edge of the dielectric wedge or the joint point of the different media is approached seeks zero according to the power law with the parameter less then one and is also poorly described by the spline (Fig.8).

(a)

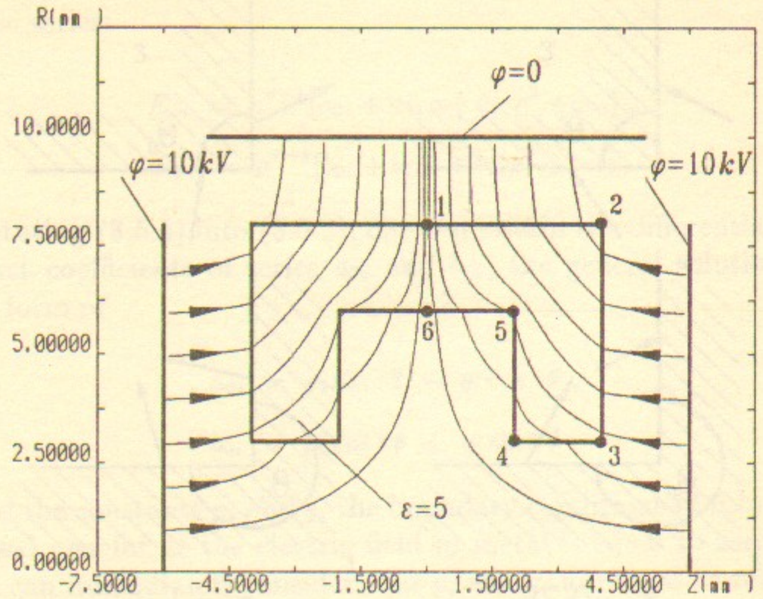

(b)

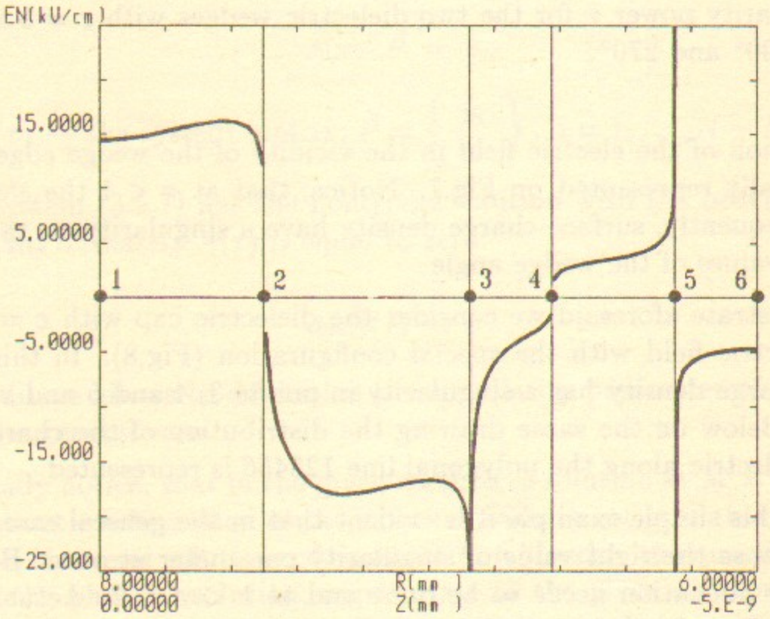

Figure 8: Dielectric cup with $\varepsilon = 5$ in the electric field: a — the geometry of the electrodes and dielectrics, the electric field force lines; b — the charge density distribution on the dielectric boundary along the polygonal line 123456.

3.6 Regularization of the magnetostatics problem

It is appropriate to consider the difficulties arising at the calculation of the magnetic focusing systems with a large magnetic constant $\mu \gg 1$. The fact is that at introducing of boundary integral equation (3.1.3) the representation of the magnetic field in the form of sum of the current field $\vec{H}_c$ and the magnetization field $\vec{H}_m$ (2.1.8) was used. But at calculation of the real magnetic systems frequently the problem of finding the small shattered magnetic fields (problem of shielding) arises. Clearly that in that case the current fields are nearly compensated by the magnetization fields. Therefore at calculation of the shielding tasks the required calculation accuracy for the each summand in (2.1.8), especially when $\mu \gg 1$ is strongly growing. But in this case, as it shown in work [5], the equation (3.1.3) becomes incorrect. Actually, let μ_2 — the magnetic constant inside of volume, limited by the contour L_m (see (3.1.3)) and $\mu_2 \gg \mu_1$. It is easy to show that a small average error at calculation of the right part of equation (3.1.3)

$$\Delta H_{\text{av}} = \frac{1}{S_m} \oint\limits_{S_m} \Big(\vec{n}(\vec{H}_c - \vec{H}_{c0}) \Big) dS \,, \tag{3.6.1}$$

therewith will lead to the significant average error in the solution of

$$\Delta\sigma_{\text{av}} = \frac{1}{S_m} \oint\limits_{S_m} (\sigma - \sigma_0) dS = \frac{\mu_2 - \mu_1}{2\mu_1} \frac{\Delta H_{\text{av}}}{2\pi} \tag{3.6.2}$$

where $\vec{H}_{c0}$ — the exact value of the current field; σ_0 — the corresponding solution of the equation (3.1.3).

Work [5] describes also the method of the initial integral equation (3.1.3) regularization by introduction in it of the additional information about solution. In our case it is the equality to zero of the total magnetic charge:

$$\oint\limits_{S_m} \sigma dS = 0 \,. \tag{3.6.3}$$

Based on this condition, equation (3.1.3) is transformed into the following form:

$$2\pi\frac{\mu_2+\mu_1}{\mu_2-\mu_1}\sigma(\xi) - \oint\limits_{L_m}\sigma(\eta)\left[\frac{\partial G}{\partial n_\xi}(\xi,\eta(l)) - \frac{1}{S_m}\oint\limits_{L_m}\frac{\partial G}{\partial n_\xi}(\xi,\zeta(l'))dl'\right]dl =$$

$$= (\vec{n}_\xi\cdot\vec{H}_c(\xi))\,, \quad \xi\in L_m\,. \tag{3.6.4}$$

Here S_m — the total magnetic surface; $\zeta=(r',z')$ — the running coordinates, belonging to the element of the magnetic contour dl'.

The equation (3.6.4) offers several advantages over the equation (3.1.3). Firstly, any one of its solutions satisfies to the condition (3.6.3). Secondly, the average solution error because of the of the right part calculation discrepancy:

$$\Delta\sigma_{\text{av}} = \frac{\mu_2-\mu_1}{\mu_2+\mu_1}\frac{\Delta H_{\text{av}}}{2\pi}\,. \tag{3.6.5}$$

However, it might be well to point out the following feature of the problem of calculation of the magnetic systems with a symmetry about plane $z=$ const. For the elements of this system, that are crossed by the plane of symmetry, the solution needs to be found only in the one half. Then in view of the antisymmetry of the magnetic charges the condition (3.6.3) will be satisfied automatically and the boundary equation (3.1.3) will look like:

$$2\pi\frac{\mu_2+\mu_1}{\mu_2-\mu_1}\sigma(\xi) - \int\limits_{L_m/2}\sigma(\eta)\left[\frac{\partial G}{\partial n_\xi}(\xi,\eta) - \frac{\partial G}{\partial n_\xi}(\xi,\tilde{\eta})\right]dl =$$

$$= (\vec{n}_\xi\cdot\vec{H}_c(\xi))\,, \quad \xi\in L_m/2\,. \tag{3.6.6}$$

where $\tilde{\eta}$ — coordinates, symmetric to the coordinates $\eta=(r,z)$.

It is easy to show that the equation (3.6.6) has the same properties as the equation (3.6.4). Hence, at a calculation of the symmetric magnetic focusing systems with the symmetric exciting currents regularization of the equation (3.6.6) is not required for the elements that are crossed by the symmetric plane. For all the other elements of given system and for all the elements of the non-symmetric magnetic systems or geometrical symmetric magnetic systems with the antisymmetric currents the calculation must be carried out using the regularized boundary condition of the equation (3.6.4). The modifications in algorithm therewith are slight and detailed adduced in Appendix A.3.

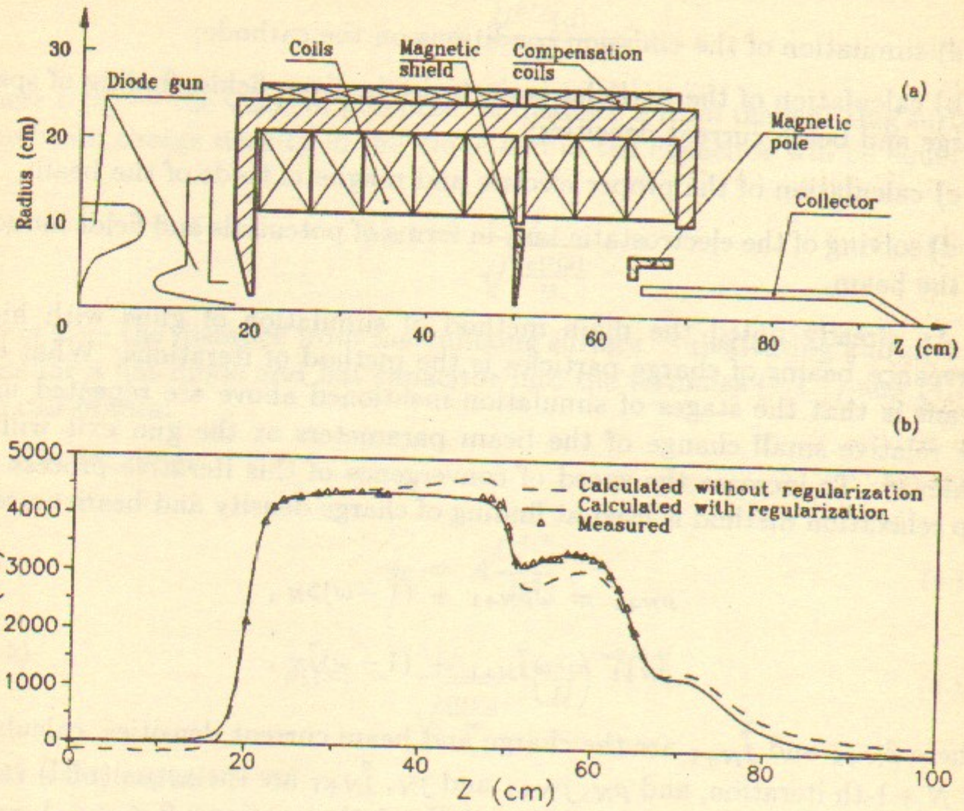

Figure 9: Magnetic system of the RF amplifier "Magnicon" : a — the magnetic shield and current wires geometry; b — the magnetic field distribution on the system axis.

Fig. 9 represents as an example the geometry and calculation results for a non-symmetric magnetic accompanying system of the 7 GHz Magnicon [6] without regularization and with regularization of the initial integral equation (3.1.3). The results of measurements, represented by I.G. Makarov, are adduced there for comparison. It is visible that the advantages of regularization present just at calculation of small shattered magnetic fields ($\mu=10^3$).

4 Dynamics of the high-perveance beam

The numerical simulation of dynamics of the high-perveance stationary beam of charge particles is included by four main stages:

a) simulation of the emission conditions on the cathode;

b) calculation of the particles trajectories in given fields, finding of space charge and beam current densities;

c) calculation of the proper electric and magnetic fields of the beam;

d) solving of the electrostatic task in terms of potentials and fields induced by the beam.

As already noted the main method of simulation of guns with high-perveance beams of charge particles is the method of iterations. What this means is that the stages of simulation mentioned above are repeated until the relative small change of the beam parameters at the gun exit will be achieved. To increase the speed of convergence of this iterative process the top relaxation method is used at finding of charge density and beam current:

$$\rho_{N+1} = \omega\tilde{\rho}_{N+1} + (1-\omega)\rho_N ,$$
$$\vec{j}_{N+1} = \omega\tilde{\vec{j}}_{N+1} + (1-\omega)\vec{j}_N , \qquad (4.0.1)$$

where $\tilde{\rho}_{N+1}$ and $\tilde{\vec{j}}_{N+1}$ are the charge and beam current densities, calculated at $N+1$-th iteration, and ρ_N, ρ_{N+1} and $\vec{j}_N$, $\vec{j}_{N+1}$ are the actual(real) values of the charge and current at N-th and $N+1$-th iterations; $0 < \omega < 1$ — the relaxation coefficient.

4.1 Initial approximation of Poisson iterations

The speed of convergence of the iterative process (4.0.1) essentially depends on the initial approximation, accepted for the beam parameters, which are unknown in the beginning of calculation. The only task can be resolved at once is the electrostatic task without considering of the space charge influence. Usually just its solution is used for finding of the beam current and particles trajectories at the first iteration. But the beam parameters found by this means differ widely from the true solution of self-consistent task.

To illustrate the foregoing we compare solutions for flat diode and flat capacitor with identical gapes D and accelerating voltage U_0. However, we anticipate that the beam of charge particles is also emitted and travels in the capacitor. For finding of the beam current density in the diode and in the capacitor we will consider that at some small distance $d \ll D$ from the emitting surface (its potential is set equal to zero) the Child's law is obeyed:

$$j = A \cdot \frac{U^{3/2}(d)}{d^2} , \qquad (4.1.1)$$

where $U(d)$ — the value of potential on distance d from the emitting surface. The beam charge density in the diode and in the capacitor will be equal to

$$\rho(x) = \frac{j}{\sqrt{\frac{2eU(x)}{m}}} , \qquad (4.1.2)$$

where x — the distance from the emitting surface. Substituting known solutions for a flat diode and flat capacitor into the formulas (4.1.1) and (4.1.2) one can obtain:

a) a flat diode

$$j_1 = A\frac{U_0^{3/2}}{D^2} , \qquad (4.1.3)$$

$$\rho_1(x) = \frac{j_1}{\sqrt{\frac{2eU_0}{m}}} \cdot \left(\frac{x}{D}\right)^{-2/3} ; \qquad (4.1.4)$$

a) a flat capacitor

$$j_2 = A\frac{U_0^{3/2}}{D^2}\left(\frac{d}{D}\right)^{-1/2} , \qquad (4.1.5)$$

$$\rho_2(x) = \frac{j_2}{\sqrt{\frac{2eU_0}{m}}} \cdot \left(\frac{x}{D}\right)^{-1/2} ; \qquad (4.1.6)$$

It is clear that solutions (4.1.5)—(4.1.6) differ widely from the true solutions (4.1.3)—(4.1.4). Especially notice the dependence of current density in capacitor from the small parameter d/D, and it always larger then current density in diode by the factor of $(D/d)^{1/2} \gg 1$. The beam charge density distributions also differ widely. In the Fig.10 *a*, *b* the dependencies of a ratio j_2/j_1 from parameter d/D and a ratio ρ_2/ρ_1 from parameter x/D at $d = D$ are shown.

From this simple example it is clear, that the use of the electrostatic task solution without considering space charge for finding of the beam parameters at the first iterations can lead not only to the large initial error and long

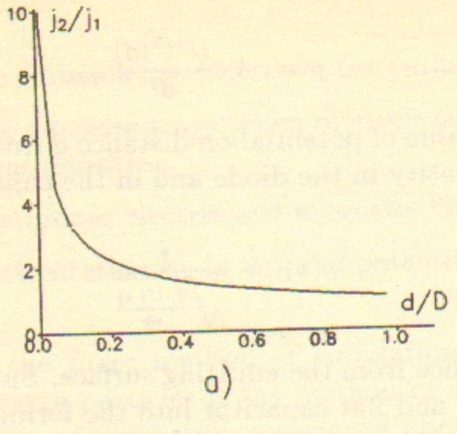

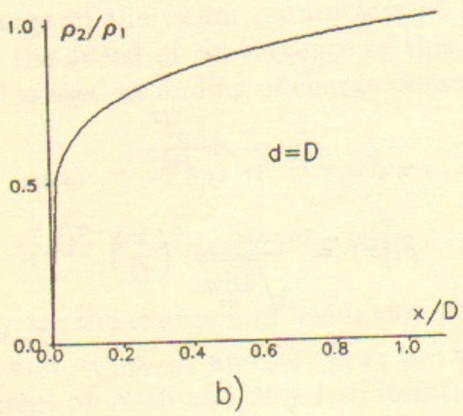

Figure 10: Comparative characteristics of the flat diode and flat capacitor.

convergence of iterations (4.0.1), but even to the beam cut-off after the first iteration. This may be overcome through the choice of relaxation factor $\omega < (d/D)^{1/2} \ll 1$, that also reduces the speed of convergence of iterations (4.0.1). Notice that in considered example the particles trajectories coincide whether the space charge influence is taken into account or not. In real guns in these two cases they differ widely, that leads to the more greater error in the initial approximation. Especially strong this problem arises at calculation of the guns with large perveance $P_\mu > 1\ \frac{\mu A}{V^{3/2}}$.

Given work proposes the other way of setting of the initial approximation of Poisson iterations. We assume, that following three parameters are known in advance:

1) the beam current I_0;

2) the effective anode–cathode gap D_0, within the limits of which the potential distribution approximately coincides with the distribution in a flat or spherical (according to the cathode form) diode with the same gap;

3) accelerating voltage U_0, acting on the beam in the gap D_0.

The current density on the cathode will be assumed or constant, or proportional to $E_0^{3/2}$, where E_0 — field on the cathode without considering the space charge. The chose of one or other distribution depends on the specific gun geometry and operating mode. Irrespective of the relative distribution of current density on the cathode the total beam current will be assumed given and equal to I_0. Further we well assume that within the limits of the gap D_0 the beam travels in the field of a flat or spherical diode with the same anode–cathode gap and accelerating voltage U_0. Once the beam particles have passed the gap D_0 and gained the energy $W = eU_0$, it is agreed that they travel with the constant energy along trajectories parallel to the gun axis (Fig. 11).

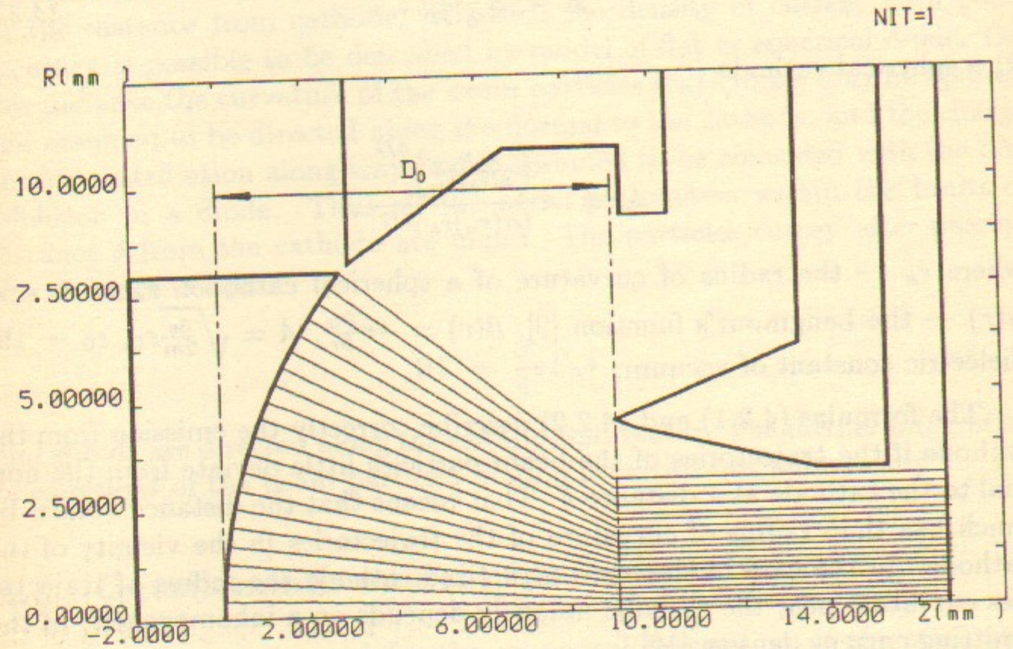

Figure 11: Trajectories of the electrons at the first iteration.

This initial approximation together with the method of top relaxation allows to reduce considerably the number of iterations on space charge required for calculation of the gun with the given accuracy. Especially that is concerned with the high-perveance guns. Besides it let us to choose the

value of relaxation coefficient arbitrarily and thereby to increase the speed of convergence of iterations.

4.2 Simulation of emission from the cathode

Emission from the cathode at all iterations on space charge, except for the first, can be described to sufficient accuracy using the model of a flat or spherical diode according to the cathode form. To do this the value of the normal to the cathode component of the electric field E_n is found at some small distance δ from the cathode (in terms of the own beam field). Then the density of current emitting from the cathode can be found by the Child–Langmour–Bloudgett's law:

1) a flat cathode

$$j_0 = A\frac{E_n^{3/2}}{\delta^{1/2}}\ ; \qquad (4.2.1)$$

2) a spherical cathode

$$J_0 = A\frac{\left(\frac{r_a E_n}{\beta(r_a)r_k}\right)^{3/2}}{(\alpha(r_a)r_k)^{1/2}}\ , \qquad (4.2.2)$$

where r_k — the radius of curvature of a spherical cathode: $r_a = r_k - \delta$; $\alpha(r)$ — the Lengmour's function [9]; $\beta(r) = -r\frac{\partial\alpha}{\partial r}$, $A = \sqrt{\frac{3e}{2m}}\varepsilon_0$, ε_0 — the dielectric constant of vacuum.

The formulas (4.2.1) and (4.2.2) describe correctly the emission from the cathode if the trajectories of the beam particles little deviate from the normal to the cathode at a distance δ. That means that the distance δ must be much less than radius of curvature of the trajectories in the vicinity of the cathode. In the case of the non-magnetized cathode the radius of trajectories curvature near the cathode uniquely depends on a inhomogeneity of the emitting current density [10]:

$$\delta \ll R_c = 5\left|\frac{j_0}{\partial j_0/\partial l}\right|\ , \qquad (4.2.3)$$

where l — the coordinate along the cathode surface.

If there is a magnetic field on the cathode, as it follows from the results of work [11], to the condition (4.2.3) one more condition is added:

$$\delta \ll \zeta_0 = \frac{c^2 j_0}{H_0\omega^2} = 3.65\cdot 10^6\frac{j_0(A/cm^2)}{H_0^3(Gs)}(cm)\ , \qquad (4.2.4)$$

where j_0 — the current density on the cathode; H_0 — the magnetic field on the cathode; $\omega = \mu_0\frac{eH_0}{m}$ — the cyclotron frequency.

The formulas (4.2.1)—(4.2.4) are true only in the immediate vicinity from the cathode, therefore the value of δ must be small in comparison with the effective anode–cathode gap, assumed at setting of the initial distribution:

$$\delta \ll D_0\ . \qquad (4.2.5)$$

The equations (4.2.3)—(4.2.5) completely define the restrictions imposed on the distance from cathode, on which the density of current with good accuracy is possible to be described by model of flat or spherical diode. On this distance the curvature of the beam particles trajectories may be ignored and assumed to be directed along the normal to the cathode, and the charge density distribution along trajectories assumed to be coincided with the distribution in a diode. Thus all the beam parameters within the limits of distance δ from the cathode are found. The particles energy after passing this distance is equal:

$$W_0 = \frac{3}{4}eE_n\delta\ , \qquad (4.2.6)$$

and speeds are directed along the electric field vector. The further integration of equations of the beam particles motion is carried out numerically.

4.3 Quasilaminar model of the current pipes

The most adequate model for the numerical description of the stationary beams of charge particles with no collisions the model of current pipes [12]. There are some versions of this model that differ in the charge particles flow dividing into the separate current pipes as well as in the charge and current distribution inside the pipe.

In the presented work the quasilaminar model of the current pipes has been developed and is used for description of the real charge particles flows

in the electron guns. In this model the current pipes are formed as follows. The cathode contour is divided into the intervals h_i, $i = 1, \ldots, N$, where N — the number of the current pipes. The trajectories of particles are released from the extreme(end) points of the intervals, a total of $N + 1$ trajectories. Each two adjacent trajectories form the one current pipe. The main feature of given model is the final size of the current pipe, which is defined by the distance between these two trajectories irrespective of their further mutual arrangement. In the case of non-laminar flow the boundary trajectories of different current pipes can be mutually intersected.

For the definition of the current carried by each pipe the linear interpolation of a current density on the cathode is used. As a result one can receive:

a) flat cathode

$$\Delta I_i = \pi h_i \left[(j_i + j_{i+1}) R_i + \frac{j_i + 2j_{i+1}}{3} h_i \sin\beta \right] ; \qquad (4.3.1)$$

b) spherical cathode

$$\Delta I_i = 2\pi R_c \mathrm{sign}(\Delta\alpha) \left\{ \frac{j_i + j_2}{2} R_0 \Delta\alpha + \right.$$

$$\left. + \left[j_i \cos\alpha_i - j_{i+1} \cos\alpha_{i+1} + \frac{j_{i+1} - j_i}{\Delta\alpha} (\sin\alpha_{i+1} - \sin\alpha_i) \right] \cdot R_c \right\} , \qquad (4.3.2)$$

where j_i and R_i — the current density and radius in the initial point of i-th trajectory; β — the angle of inclination of the straight line forming a flat cathode contour; R_0 and R_c – the radius of the center and radius of the curvature of the circle forming the contour of a spherical cathode; α_i — the angle between the system axis and the straight line connecting the center of this circle with the initial point of the i-th trajectory, $\Delta\alpha = \alpha_{i+1} - \alpha_i$, $i = 1, \ldots, N$.

The particles trajectories are found by the numerical integration of the equation of movement (2.2.2), the components of which in the axial-symmetric case take the form of:

$$\frac{dP_r}{dt} = \frac{P_\theta V_\theta}{r} + e \left(E_r + \frac{V_\theta}{c} B_z - \frac{V_z}{c} B_\theta \right) ,$$

$$\frac{dP_z}{dt} = e \left(E_z + \frac{V_r}{c} B_\theta - \frac{V_\theta}{c} B_r \right) ,$$

$$\frac{d(P_\theta \cdot r)}{dt} = er \left(\frac{V_z}{c} B_r - \frac{V_r}{c} B_z \right) , \qquad (4.3.3)$$

where $V_\theta = r\dot{\theta}$.

To describe the space charge and current of the beam the set of rectangular grids continuously filling the assumed area of the beam movement in the plane (r, z) is introduced. Each of grids may have the arbitrary sizes and division into rectangular cells. Within the limits of one cell of the grid the charge and current densities are assumed to be constant ones. The set of various grids is necessary for exact description of the strong inhomogeneity of a beam charge density in the vicinity of the cathode as well as inhomogeneity of a charge and current density at high beam compression.

The beam current and space charge are distributed over the mesh cells as follows. The trajectories calculation is carried out in parallel, so that they always intersected only the same vertical mesh cells layer. Thus each layer has the following parameters of trajectories: $R_i^{(1,2)}$ — the radiuses of inlet (1) and outlet (2); $\Delta t_i = t_i^{(2)} - t_i^{(1)}$ — the moving time in the layer. The current pipes borders in each layer are the cylinders of radius

$$R_i = \frac{R_i^{(1)} + R_i^{(2)}}{2} , \qquad i = 1, \ldots, N+1 . \qquad (4.3.4)$$

The charge delivered by each of current pipes into the given layer, is equal to

$$Q_i = \Delta I_i \cdot \frac{\Delta t_i + \Delta t_{i+1}}{2} , \qquad if\ \Delta t_i \cdot \Delta t_{i+1} \neq 0 ,$$

$$Q_i = 0 , \qquad if\ \Delta t_i \cdot \Delta t_{i+1} = 0 , \qquad i = 1, \ldots, N , \qquad (4.3.5)$$

where ΔI_i — the pipe current determined by the formulas (4.3.1) or (4.3.2).

The charges in all the cells of the given mesh layer will be equal to

$$Q_m = \sum_{i=1}^{N} \frac{Q_i}{V_i} V_{im} , \qquad m = 1, \ldots, M , \qquad (4.3.6)$$

where $V_i = \pi |R_{i+1}^2 - R_i^2| \cdot \delta z$ — the volume, occupied by the i-th current pipe in the given mesh layer of thickness Δz; V_{im} — the volume, occupied by the i-th current pipe in the m-th cell in this layer; M — the total number of cells in the given layer.

The advantages of the described quasilaminar model, as we believe, consist in opportunity to describe with sufficient accuracy just as strongly nonlaminar beams, so also the beams with a high compression with a relative small number of the current pipes.

4.4 Calculation of potentials and fields induced by the beam

During integration of equations of movement (4.3.3) it is necessary to know the values of the electric and magnetic fields, including the induced by the beam ones, in the whole area of the beam particles movement. In addition, solving of electrostatic task it is necessary to known the values of the electric potentials and fields, induced by the beam on the electrodes and dielectrics surfaces, consequently (see 3.2.13).

The additive to electrostatic potential at the expense of the beam space charge, according to the equation (2.1.4), has the following form:

$$\varphi_\rho(\vec{r}_0) = \int\limits_{V_b} \frac{\rho(\vec{r})dV}{|\vec{r}_0 - \vec{r}|} . \qquad (4.4.1)$$

Having regard to the axial symmetry of a task and accepted assumption about the charge density uniformity within the limits of the one mesh cell, the integral (4.4.1) can be written in the form

$$\varphi_\rho(\xi) = \sum_{i=1}^{M} \rho_i \int\limits_{S_i} G(\xi,\eta)dS , \qquad (4.4.2)$$

where $\xi = (r_0, z_0)$ — the coordinates of the point of observation; $\eta = (r, z)$ — the running coordinates; the function $G(\xi,\eta)$ is defined by the formula (3.1.4); ρ_i — the charge density in the i-th cell, S_i — its cross-section, and M — the total number of cells in all the meshes.

The electric field of the beam space charge from the formula (4.4.2), can be written in the form

$$\vec{E}_\rho(\xi) = -\vec{\nabla}_\xi \varphi_\rho(\xi) = -\sum_{i=1}^{M} \rho_i \int\limits_{S_i} \vec{\nabla}_\xi G(\xi,\eta)dS , \qquad (4.4.3)$$

where the function $\vec{\nabla}_\xi G(\xi,\eta)$ is defined by the formulas (3.1.7) and (3.1.8).

For the beam magnetic field from the formulas (2.1.7) we obtain the following expression in cylindrical coordinates:

$$B_\theta(\xi) = \frac{1}{2cr_0} \int\limits_0^{r_0} j_z(r, z_0) r dr . \qquad (4.4.4)$$

The electric potentials and fields induced by the beam are expressed by the integrals of form

$$\varphi_i(\xi) = \int\limits_{S_i} G(\xi,\eta)dS , \qquad (4.4.5)$$

$$\vec{E}_i(\xi) = -\int\limits_{S_i} \vec{\nabla}_\xi G(\xi,\eta)dS , \qquad (4.4.6)$$

which represent the potential and electric field, produced in the point of observation by the charge in the i-th cell with unit density $\rho_i = 1$. There is no analytical expression for the integrals (4.4.5)—(4.4.6) in the general case, therefore they are calculated numerically. Notice, however, that functions under the integrals in (4.4.5)—(4.4.6) have singularities if the point of observation is inside or on the boundary of the i-th mesh cell. Hence the accuracy of numerical calculation sharply drops. At calculation of the integral (4.4.5) it happens when the electrode intersects the mesh cell or is tangent to it, and it demands to find the potential on it induced by the charge of this cell (for example, a spherical cathode always intersects the rectangular mesh cells). Besides the electric and magnetic fields are calculated only in the mesh nodes. Field over all area of the beam movement are found then using the parabolic interpolation over the values of fields in the nine nearest mesh nodes. Therefore the set of different meshes is necessary and for more exact description of the strong non-uniform fields (for example, electric field in the vicinity of anode aperture). However, at calculation of the electric field, produced by the individual mesh cell charge in nodes, coincided with the vertexes of this cell, the function under the integral in (4.4.6) also has the singularity.

To separate the singularity of functions under integrals in (4.4.5)—(4.4.6) we proceed the same way as at allocation of the kernel singularity of the integrated equations (see the formula (3.3.1)). We designate through $\tilde{G}(\xi,\eta)$ and $\vec{\nabla}_\xi \tilde{G}(\xi,\eta)$ the asymptotics of the functions under the integrals at $\eta \to$

ξ. In this case, accurate to the sign, they coincide with the potential and electric field of infinitely thin filament with the unit linear charge density. The integrals (4.4.5)—(4.4.6) can be rewritten in the form

$$\varphi_i(\xi) = \int\limits_{S_i} \left[G(\xi,\eta) - \tilde{G}(\xi,\eta)\right] dS + \int\limits_{S_i} \tilde{G}(\xi,\eta) dS$$

$$-\vec{E}_i(\xi) = \int\limits_{S_i} \left[\vec{\nabla}_\xi G(\xi,\eta) - \vec{\nabla}_\xi \tilde{G}(\xi,\eta)\right] dS + \int\limits_{S_i} \vec{\nabla}_\xi \tilde{G}(\xi,\eta) dS \,. \qquad (4.4.7)$$

The first integrals in (4.4.7) have no allocations and can be calculated numerically with a good accuracy, the second are calculated analytically (see Appendix A.4). The described procedure of singularity allocation provides the poor accuracy if the point of observation is on the gun axis. However, in this case the integrals (4.4.5)—(4.4.6) can be calculated analytically. The results of these calculations are also adduced in Appendix A.4.

Notice, that the accuracy of calculation of the own fields appreciably drops on the beam boundary. There are two reasons for that.

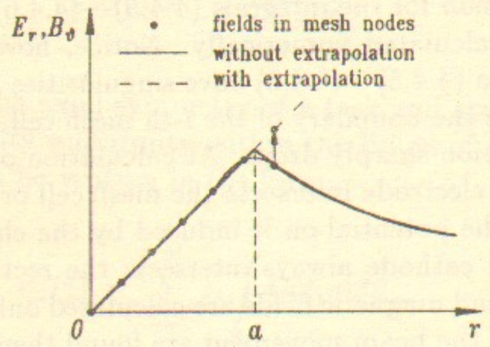

Figure 12: Beam own fields versus the radius (a — the beam radius).

Firstly, as a rule, the beam in an electron gun has a sharp boundary – the charge density becomes zero on the distance from a boundary, much less than the beam cross-size. This distance is defined by the beam cross phase volume and at calculation is usual assumed to be zero. In this case the own beam fields have a brake on the boundary. If the beam boundary is not parallel to the gun axis and does not pass through the mesh nodes, this leads to errors in calculation of the own beam fields inside the mesh cell, containing the boundary because of using of interpolation (see Fig. 12). One

can see from the drawing that the field in the vicinity of the boundary appears to be less than true one. As a result the extreme trajectories experience a less defocusing action of the space charge and fall inward the beam. This artificial aberration is typical of the many existing computing algorithms for descriptions of the space charge flows.

Secondly, owing to the uniform spread along the cells, the significant part of the beam charge and current is removed out of its border. That leads to the additional reducing of the own beam fields action and gain of the described artificial aberration. These errors especially have an effect at calculation of extended beams and beams with high area compression.

In this case developed by us algorithm of the beam own fields extrapolation allows to increase the calculation accuracy significantly. For this purpose at first from the formulas (4.4.3)—(4.4.4) the field values in the mesh nodes inside the beam are calculated. On the strength of axial symmetry of task in the mesh nodes in plane $z = \text{const}$, the beam own electric and magnetic fields can be presented in the form of following series:

$$E_r = \sum_{i=1}^{N} a_i r^{2i-1} \,,$$

$$E_z = \sum_{i=1}^{N} b_i r^{2i-2} \,, \qquad (4.4.8)$$

$$B_\theta = \sum_{i=1}^{N} c_i r^{2i-1} \,.$$

The coefficients a_i, b_i , c_i are found by the method of least squares over the calculated fields values in the mesh nodes inside the beam. In the mesh nodes, located outside of the beam, the own fields are already calculated from the formulas (4.4.8). The effect of the applying of the described algorithm will be shown below on example of calculation of the real electron gun.

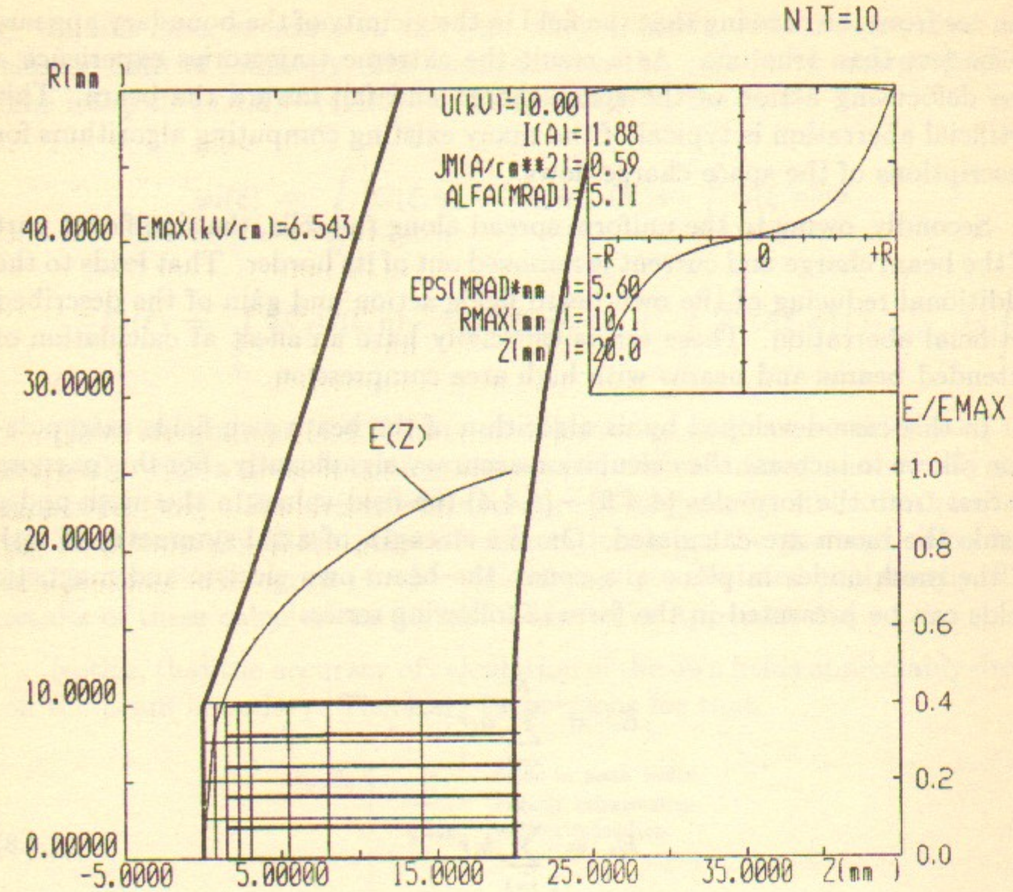

Figure 13: Pierce gun with a flat cathode (the gap between the gun anode and cathode is equal to the cathode diameter, microperveance $P_{\mu 0} = 1.83\ \mu A/V^{3/2}$).

5 Tests and examples of the electron guns calculation

5.1 Test calculation of electron guns

The first test is calculation of the axial-symmetric Pierce gun with a flat cathode. The gap between the gun anode and cathode was chosen equal to the cathode diameter (microperveance $P_{\mu 0} = 1.83\ \mu A/V^{3/2}$). The gun electrodes geometry was calculated numerically by the method, described in work [9], and is shown in Fig.13. To describe the beam space charge three

meshes at three division variants of each of the meshes into the cells were used. In Fig.13 the meshes structure in the initial variant with the total number of mesh cells of $N_{\text{cell}} = 32$ is shown. Two other variants were different from the initial one by increase of cells number in each mesh along the radius and gun axis by a factor of two and three. The distance from the cathode, on which the beam was described by the model of a flat diode (see section 4.2), in all the three variants was identical and equal to the two longitudinal sizes of the mesh cell next to the cathode in the initial variant.

The calculation results for all the three variants are shown in Tab.1, where the calculated gun microperveance and its difference from the theoretical one, current density inhomogeneity on the cathode, as well as the maximal angle of inclination of the trajectories (j_0 – the theoretical value of the current density) are mentioned.

Table 1:

N_{var}	N_{cell}	P_μ	$\frac{P_\mu - P_{\mu 0}}{P_{\mu 0}}$, %	$\frac{j_{\max} - j_{\min}}{j_0}$, %	$\alpha_{\max}$(mrad)
1	32	1.8795	2.70	1.2	5.1
2	128	1.8499	1.09	0.64	0.9
3	288	1.8416	0.63	0.42	1.4

As seen from Tab.1, the calculation errors in all the variants are sufficiently small and systematically decrease with increase of the mesh cells number. Specially notice the good solution stability even at very rough mesh. It connected with the uniform charge "spread" over the mesh cells, allocation of singularities at beam space charge field calculation, as well as with the use of parabolic interpolation for the total electric field description. In Fig.13 the received in initial variant equipotential lines and field distribution on the gun axis, as well as particles trajectories, the current density distribution and beam phase portrait at the gun output are shown.

One more test was the calculation of the Pierce gun with a spherical cathode. The convergence angle of the electron beam in the gun $\alpha_0 = 40°$ at a ratio of the cathode and anode curvature radiuses $r_k/r_a = 5$ (beam area compression ratio of 25 : 1, microperveance $P_{\mu_0} = 0.431\ \mu A/V^{3/2}$). The geometry accepted in the gun electrodes calculations that was found by the Harker method [13] is shown in Fig.14.

The beam space charge was described by the three meshes, and the three

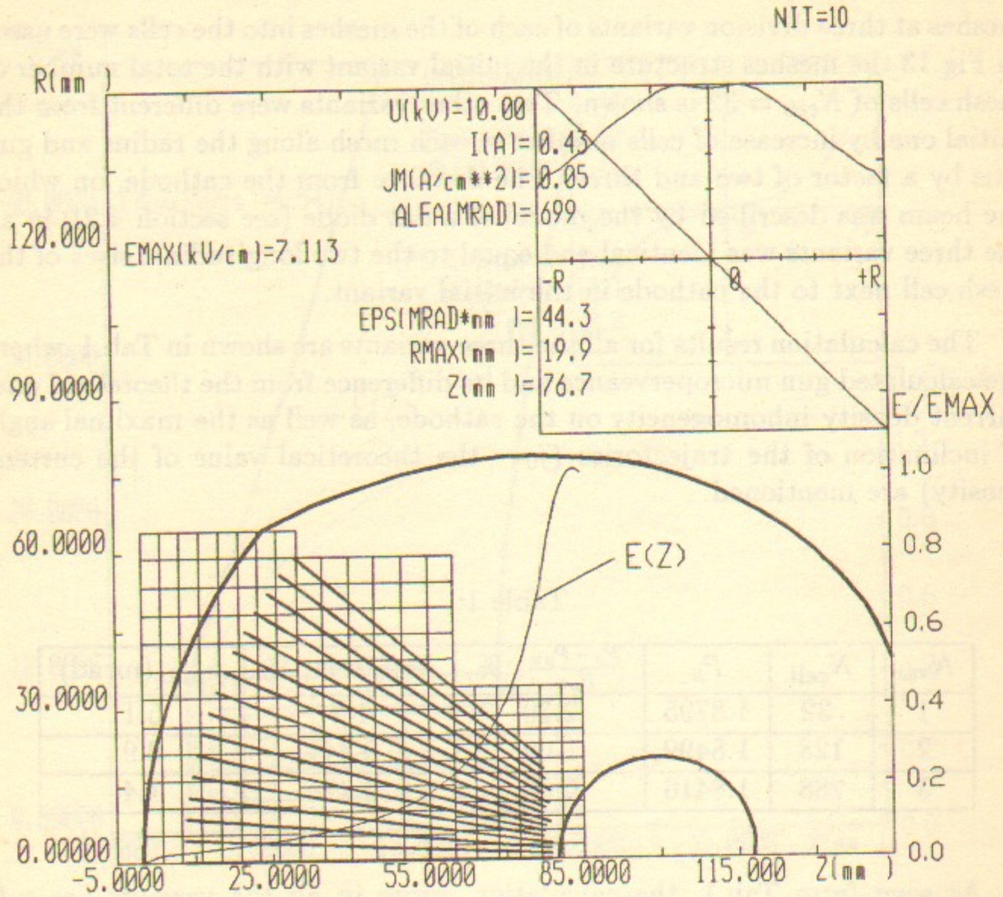

Figure 14: Pierce gun with a spherical cathode. The beam convergence angle is 40°, the ratio between the radii of the cathode and anode $r_c/r_a = 5$ (microperveance $P_{\mu 0} = 0.431\ \mu A/V^{3/2}$).

variants of the mesh dividing into cells was considered. In the initial variant the total number of cells in two meshes was equal to $N_{\text{cell}} = 60$. The two other variants were different from the initial one by increasing of the number of cells in the each mesh along the radius and gun axis in two and three times.

The first series of calculations was carried out at the fixed distance $\delta = (r_c - r_a)/10$ from the cathode, where the beam was described by the model of a spherical diode (see section 4.2). In all these three variants the value of δ was chosen equal to the maximal cell size $h = \max(\Delta r, \Delta z)$ in the mesh next to the cathode in the initial variant. The calculation results are shown in Table 2, where $\Delta\alpha_{\max}$ is the maximal difference between the calculation

value of the beam outer trajectory inclination angle and the convergence one.

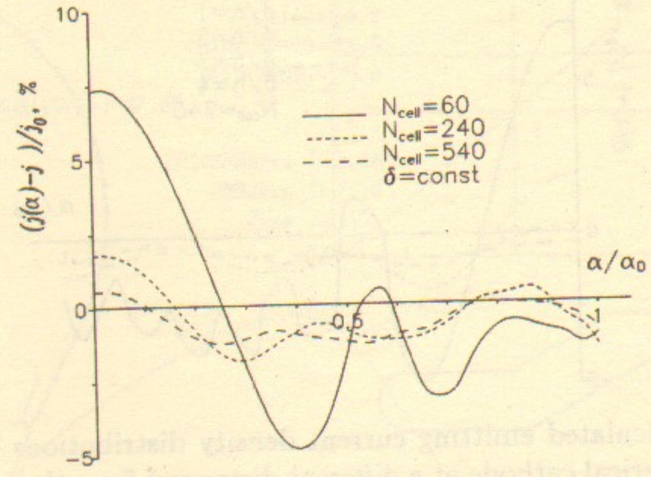

Figure 15: Calculated emitting current density distributions for the Pierce gun with a spherical cathode at different numbers of total mesh nodes.

The calculation results for the second variant are reflected also in Fig.14, where the arrangement of the mesh nodes, the calculated equipotentials, released from the mesh nodes on the gun axis, the electric field distribution along the gun axis, and particles trajectories can be seen. The distribution curves of the current density on the gun cathode (see Fig.15), normalized to the exact value of the current density j_0, show the convergence speed of the gun calculation parameters to the theoretical ones with increase of the cells number in the mesh.

Table 2:

N_{var}	N_{cell}	$\frac{\delta}{h}$	P_μ	$\frac{P_\mu - P_{\mu 0}}{P_{\mu 0}}$, %	$\frac{j_{\max} - j_{\min}}{j_0}$, %	$\frac{\Delta\alpha_{\max}}{\alpha_0}$, %
1	60	1	0.4251	-1.37	11.33	-0.17
2	240	2	0.4285	-0.58	3.55	0.07
3	540	3	0.4285	-0.58	1.86	0.09

For the second variant of mesh dividing with $N_{\text{cell}} = 240$ the dependence of the calculated gun parameters from the rate δ/h, where h is the maximal size of the mesh cell next to the cathode in this variant has also been investigated. The results of calculations are presented in Fig.16 and Tab.3.

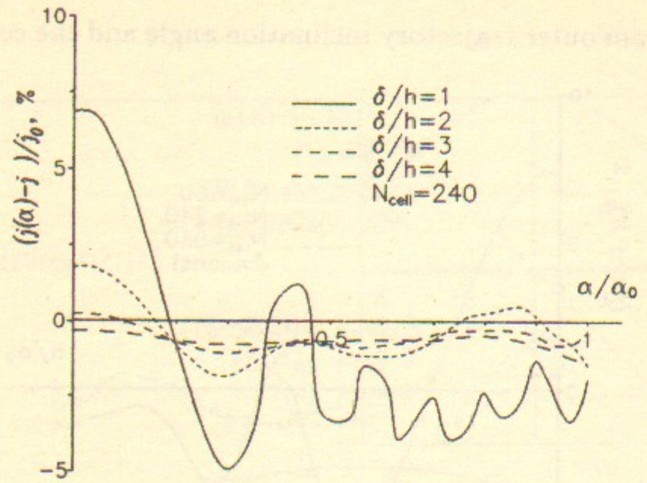

Figure 16: Calculated emitting current density distributions for the Pierce gun with a spherical cathode at a different distance δ from the cathode, where the beam are described by the spherical diode model (h — the maximal size of the mesh cell close to the cathode).

It is evident from the results of tests carried out, that for the high calculation accuracy accounts achievement it is necessary to satisfy the condition $\delta/h \geq 2$, where h is the longitudinal size of the mesh cell next to the cathode in the case of a flat cathode and the maximal size of the mesh cell next to the cathode for the cathode of the spherical form. It is the only restriction, imposed from below on the value of the parameter δ.

Table 3:

$\frac{\delta}{h}$	P_μ	$\frac{P_\mu - P_{\mu 0}}{P_{\mu 0}}$, %	$\frac{j_{max} - j_{min}}{j_0}$, %	$\frac{\Delta\alpha_{max}}{\alpha_0}$, %
1	0.4207	-2.39	11.04	-0.20
2	0.4285	-0.58	3.55	0.07
3	0.4284	-0.60	1.29	0.03
4	0.4278	-0.74	1.07	-0.01

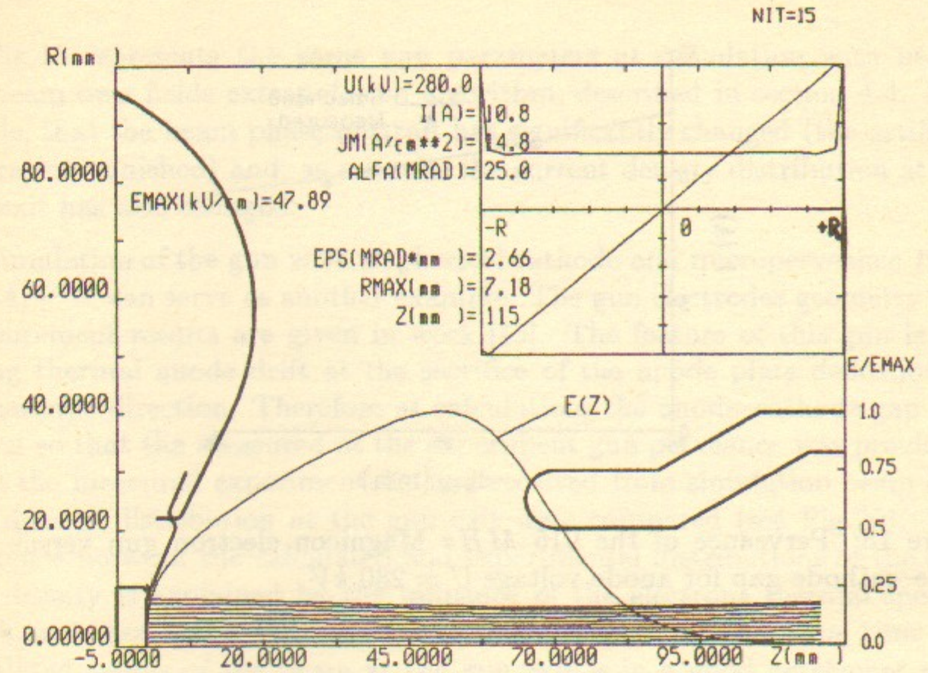

Figure 17: Electron gun of the 915 MHz RF amplifier "Magnicon."

5.2 Examples of the real electron guns simulation

The simulation of the 915 MHz RF amplifier "Magnicon" [14] electron gun can serve as one such example. The geometry of the gun cathode unit, focusing electrodes, and anode is shown in Fig.17. For the beam space charge description the seven meshes with the total number of cells $N_{\text{cell}} = 312$ were used.

One of calculation tasks were to receive the gun perveance dependence on the anode–cathode gap. The results of simulation and measurements at accelerating voltage of 280 kV are presented in Fig.18. The results of measurements are given by E.V. Kozyrev. The difference between the experimental results and calculation curve is explained by the accuracy of manufacturing and adjusting of the separate gun units as well as their thermal drift. In addition, as a result of calculations, the beam particles trajectories , its phase portrait and current density distribution at the gun exit (see Fig.17) were found. The calculated equipotentials in the beam motion area and electric field distribution on the gun axis are also shown in Fig.17.

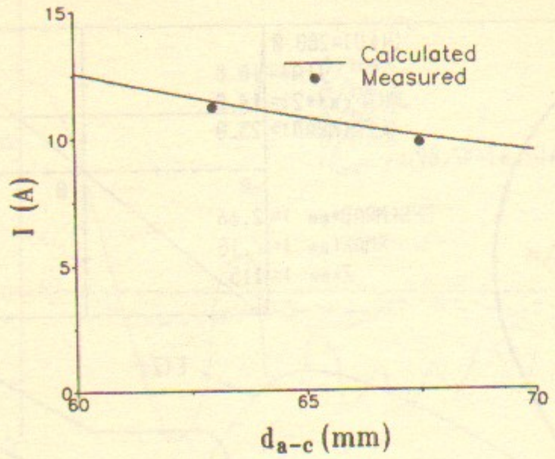

Figure 18: Perveance of the 915 MHz Magnicon electron gun versus the anode–cathode gap for anode voltage $U = 280\ kV$.

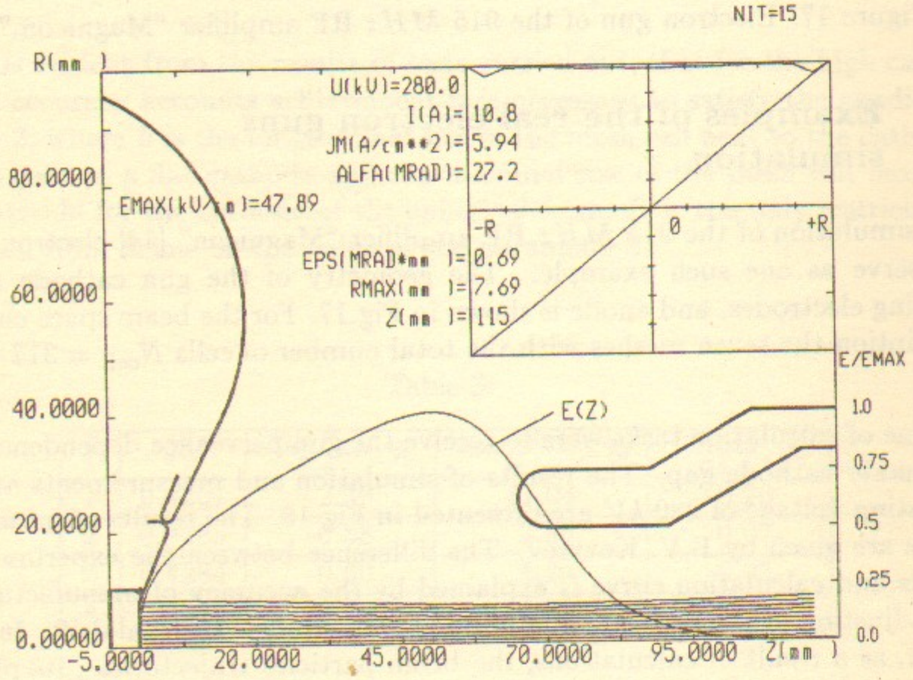

Figure 19: Electron gun of the 915 MHz RF amplifier "Magnicon," calculation with extrapolation of the beam own fields.

Fig.19 represents the same gun parameters at calculation with use of the beam own fields extrapolation algorithm, described in section 4.4. It is visible, that the beam phase portrait has significantly changed (the artificial aberration vanished) and, as a result, the current density distribution at the gun exit has also changed.

Simulation of the gun with a spherical cathode and microperveance $P_\mu = 1.9\mu A/V^{3/2}$ can serve as another example. The gun electrodes geometry and measurement results are given in work [15]. The feature of this gun is the strong thermal anode drift at the sacrifice of the anode plate deflection in the cathode direction. Therefore at calculations the anode–cathode gap was chosen so that the measured at the experiment gun perveance was provided. Thus the measured experimentally and received from simulation beam current density distribution at the gun exit were compared (see Fig.20). The difference between the calculated and experimental distributions of the current density is explained by the influence of the electrons thermal speeds, which were not taken into account at calculations. At the same time the calculated radius of the beam at the gun exit is in a good agreement with the measured in experiment one. The beam area convergence in the given example comprises $C_s = 27$.

The accepted at simulation the gun electrodes geometry and position of the collector, with help of which the beam current density distribution was measured, are shown in Fig.21. There are also the equipotentials, started from the axial mesh nodes (the total number of cells in five meshes is $N_{\text{cell}} = 376$), the electric field distribution along the gun axis, beam particles trajectories, as well as its phase portrait and current density distribution on the gun collector.

Acknowledgments

In summary the authors wish to acknowledge V.Ya. Ivanov and G.I. Kuznetsov for useful discussions, D.G. Myakishev for participation in program realization of developed algorithms and carrying out of test calculations.

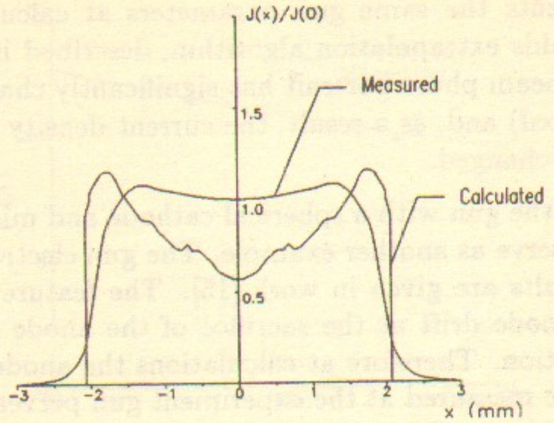

Figure 20: Current density distribution on the collector of the gun with microperveance $P_{\mu 0} = 1.9\ \mu A/V^{3/2}$ and beam area compression $C_s = 27$.

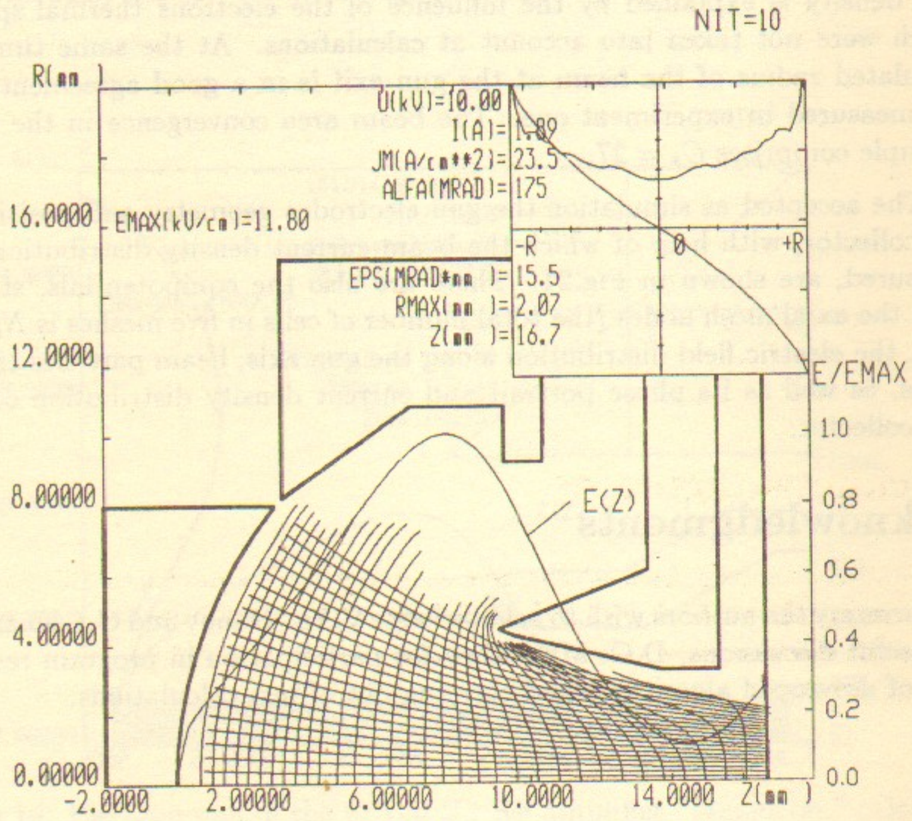

Figure 21: Geometry of the electrodes and calculated parameters of the gun with microperveance $P_{\mu 0} = 1.9\ \mu A/V^{3/2}$ and beam area compression $C_s = 27$.

A Appendices

A.1 Appendix

The kernel asymptotic at $\eta \to \xi_j$ has the following form:

a) on a metal surface

$$\tilde{R}(\xi_j, \tilde{\eta}) \;=\; (2 + \varepsilon \sin\alpha) \ln \frac{8}{\varepsilon} \;+\; \varepsilon \sin\alpha \;+\; O(\varepsilon^2)\,; \qquad \text{(A.1.1)}$$

b) on a boundary between dielectrics and magnetics

$$\tilde{R}(\xi_j, \tilde{\eta}) \;=\; \frac{\cos\alpha}{r_j} \left[1 - \left(1 + \frac{\varepsilon}{2} \sin\alpha\right) \ln \frac{8}{\varepsilon}\right] \;+\; O(\varepsilon^2)\,, \qquad \text{(A.1.2)}$$

where

$$\varepsilon \;=\; \frac{\sqrt{(r_j - \tilde{r})^2 + (z_j - \tilde{z})^2}}{r_j}\,, \qquad \text{(A.1.3)}$$

$$\sin\alpha \;=\; \frac{r_j - \tilde{r}}{\sqrt{(r_j - \tilde{r})^2 + (z_j - \tilde{z})^2}}\,; \qquad \text{(A.1.4)}$$

$\tilde{r},\ \tilde{z}$ – the coordinates on the tangent line to the contour of the electrode, dielectric or magnetic in the point $\xi_j = (r_j, z_j)$. For calculation of additional integrals in (3.3.1) we enter a new variable $x = (l - l_{j-1})/h_j$, then

$$J^m_{jj} \;=\; \int_{l_{j-1}}^{l_j} \psi_m(l) \tilde{R}(\xi_j, \tilde{\eta}(l)) dl \;=\; h_j \int_0^1 \psi_m(x) \tilde{R}(\xi_j, \tilde{\eta}(x)) dx\,, \qquad \text{(A.1.5)}$$

where $\psi_1 = (1-x)^3,\ \psi_2 = x^3,\ \psi_3 = 1 - x,\ \psi_4 = x$.

Inserting into (A.1.5) the asymptotics (A.1.1)–(A.1.2), and, considering that $\varepsilon = \frac{h_j}{r_j}(1-x)$, after awkward but simple calculations one can receive:

a) on a metal surface

$$J^1_{jj} \;=\; h_j \left[\left(\frac{1}{2} + \frac{b}{20}\right) \ln \frac{8}{a} + \frac{137}{1200} b + \frac{25}{24}\right]\,,$$

$$
\begin{aligned}
J^2_{jj} &= h_j\left[\left(\frac{1}{2}+\frac{b}{5}\right)\ln\frac{8}{a}+\frac{6}{25}b+\frac{1}{8}\right] ,\\
J^3_{jj} &= h_j\left[\left(1+\frac{b}{6}\right)\ln\frac{8}{a}+\frac{11}{36}b+\frac{3}{2}\right] ,\\
J^4_{jj} &= h_j\left[\left(1+\frac{b}{3}\right)\ln\frac{8}{a}+\frac{4}{9}b+\frac{1}{2}\right] ;
\end{aligned}
\qquad \text{(A.1.6)}
$$

b) on a boundary between dielectrics or magnetics

$$
\begin{aligned}
J^1_{jj} &= c\left[\left(\frac{1}{4}+\frac{b}{40}\right)\ln\frac{8}{a}+\frac{77}{2400}b+\frac{13}{48}\right] ,\\
J^2_{jj} &= c\left[\left(\frac{1}{4}+\frac{b}{10}\right)\ln\frac{8}{a}+\frac{b}{50}-\frac{3}{16}\right] ,\\
J^3_{jj} &= c\left[\left(\frac{1}{2}+\frac{b}{12}\right)\ln\frac{8}{a}+\frac{5}{72}b+\frac{1}{4}\right] ,\\
J^4_{jj} &= c\left[\left(\frac{1}{2}+\frac{b}{6}\right)\ln\frac{8}{a}+\frac{b}{18}-\frac{1}{4}\right] ;
\end{aligned}
\qquad \text{(A.1.7)}
$$

where $a = h_j/r_j$, $b = a\sin\alpha$; $c = -a\cos\alpha$.

If the point of observation coincides with the beginning of the segment of integration, i.e. $i = j-1$, integrals $J^m_{j-1,j}$ will be equal to integrals J^m_{jj} accurate to replacement r_j with r_{j-1} (the angle of tangent line will be also changed) and indexes modification $1 \leftrightarrow 2$ and $3 \leftrightarrow 4$.

A.2 Appendix

The integrals (3.3.1) have the following form:

$$
I^m_{ij} = h_j\int_0^1 a_{1j}(x)a_{2j}(x)\psi_m(x)R_{ij}(x)dx , \qquad \text{(A.2.1)}
$$

where

$$
a_{1j}(x) = \left(\frac{N+2\delta}{j-2+\delta+x}\right)^{1-\tau_1} ,
$$

$$
a_{2j}(x) = \left(\frac{N+2\delta}{N-j+1+\delta-x}\right)^{1-\tau_2} , \qquad \text{(A.2.2)}
$$

$\delta = d/h$ (on metal $\delta \equiv 0$); N – the number of the spline steps on the segment $0 \le l \le L_{tk}$; $h = \text{const}$ – the spline step; $\psi_m(x)$ – the weight spline functions (see the Appendix A.1;

$$
R_{ij}(x) = \begin{cases} G(\xi_i,\eta(x)) - \text{on metal} \\ \frac{\partial G}{\partial n_{\xi_i}}(\xi_i,\eta(x)) - \begin{array}{l}\text{on dielectric or}\\ \text{on magnetic}\end{array} \end{cases} \qquad \text{(A.2.3)}
$$

$l_{j-1} \le \eta(x) \le l_j$ at $0 \le x \le 1$.

In the formula (3.4.7) the second integral will be equal to ($\delta \equiv 0$)

$$
\int_0^1 P_j(x)dx = \int_0^1 \left(\frac{N}{x}\right)^{1-\tau} = \frac{N^{1-\tau}}{\tau} , \qquad \text{(A.2.4)}
$$

where $\tau = \tau_1$ at $j = 2$ and $\tau = \tau_2$ at $j = N$.

In the formula (3.4.9) the second integrals will have the following form

$$
J^m_{ij} = \int_0^1 P_j(x)Q_m(x)\tilde{R}_{ij}(x)dx = h\int_0^1 \left(\frac{N}{x}\right)^{1-\tau}\psi_m(x)\tilde{R}_{ij}(x)dx , \qquad \text{(A.2.5)}
$$

where $\tilde{R}_{ij}(x) = \tilde{R}(\xi_i,\tilde{\eta}(x))$ (see Appendix A.1). The integrals (A.2.5) are the same at $j = 2$ and $j = N$ accurate to replacement(substitution) of τ_1 with τ_2 and of the weight functions with $m = 1$ and $m = 3$ with $m = 2$ and $m = 4$ and vice versa. Therefore we write out the results only for $j = N$:

$$
\begin{aligned}
J^1_{NN} &= N^{1-\tau}h\left[(2a_1+a_2b)\ln\frac{8}{a}+(a_{22}+a_2)b+2a_{12}\right] ,\\
J^2_{NN} &= N^{1-\tau}h\left[\left(\frac{2}{\tau+3}+\frac{b}{\tau+4}\right)\ln\frac{8}{a}+\frac{\tau+5}{(\tau+4)^2}b+\frac{2}{(\tau+3)^2}\right] ,\\
J^3_{NN} &= N^{1-\tau}h\left[(2b_1+b_2b)\ln\frac{8}{a}+(b_{22}+b_2)b+2b_{12}\right] ,\\
J^4_{NN} &= N^{1-\tau}h\left[\left(\frac{2}{\tau+1}+\frac{b}{\tau+2}\right)\ln\frac{8}{a}+\frac{\tau+3}{(\tau+2)^2}b+\frac{2}{(\tau+1)^2}\right] ,
\end{aligned}
\qquad \text{(A.2.6)}
$$

where the following designations were entered:

$$
\begin{aligned}
a &= \frac{h}{r_N}, \quad b = a\sin\alpha\,, \\
a_1 &= \frac{1}{\tau} - \frac{3}{\tau+1} + \frac{3}{\tau+2} - \frac{1}{\tau+3}\,, \\
a_{12} &= \frac{1}{\tau^2} - \frac{3}{(\tau+1)^2} + \frac{3}{(\tau+2)^2} - \frac{1}{(\tau+3)^2)}\,, \\
a_2 &= \frac{1}{\tau+1} - \frac{3}{\tau+2} + \frac{3}{\tau+3} - \frac{1}{\tau+4}\,, \\
a_{22} &= \frac{1}{(\tau+1)^2} - \frac{3}{(\tau+2)^2} + \frac{3}{(\tau+3)^2} - \frac{1}{(\tau+4)^2)}\,, \\
b_1 &= \frac{1}{\tau} - \frac{1}{\tau+1}\,, \\
b_{12} &= \frac{1}{\tau^2} - \frac{1}{(\tau+1)^2}, \\
b_2 &= \frac{1}{\tau+1} - \frac{1}{\tau+2}\,, \\
b_{22} &= \frac{1}{(\tau+1)^2} - \frac{1}{(\tau+2)^2}\,,
\end{aligned}
\qquad \text{(A.2.7)}
$$

It is easy to see that at $\tau = 1$ the integrals (A.1.6) coincide with integrals (A.2.6) from Appendix A.1.

In the formula (3.4.10) the second integral coincides with the integral (A.2.4), and the third has the following form:

$$
\int\limits_0^1 \tilde{R}_{ij}(x)dx = \int\limits_0^1 \left[\left(2 + x\frac{h_j}{r_i}\sin\alpha\right)\ln\frac{8r_i}{h_j x} + x\frac{h_j}{r_i}\sin\alpha\right]dx\,.
$$

Designating $a = h_j/r_i$, $b = a\sin\alpha$, we receive

$$
\int\limits_0^1 \tilde{R}_{ij}(x)dx = \left(2 + \frac{b}{2}\right)\ln\frac{8}{a} + \frac{b}{2} + \frac{5}{4}\,. \qquad \text{(A.2.8)}
$$

The additional integrals in formulas (3.4.14)–(3.4.15) are the same at $j = 2$

and $j = N$ accurate to replacement of τ_1 with τ_2. Therefore the results only for $j = N$ are offered:

$$
\int\limits_1^{1+\delta} P_N(x)dx = \int\limits_1^{1+\delta}\left(\frac{N+2\delta}{1+\delta-x}\right)^{1-\tau}dx = \left(\frac{N+2\delta}{\delta}\right)^{1-\tau}\frac{\delta}{\tau}\,, \qquad \text{(A.2.9)}
$$

$$
\int\limits_1^{1+\delta} P_N(x)\tilde{R}_{iN}(x)dx =
$$

$$
= \left(\frac{N+2\delta}{\delta}\right)^{1-\tau} d\left[\left(\frac{2}{\tau} + \frac{a}{\tau+1}\right)\ln\frac{8r_i}{d} + \frac{\tau+2}{(\tau+1)^2}a + \frac{2}{\tau^2}\right]. \qquad \text{(A.2.10)}
$$

Here $d = \delta h$ and $a = (d/r_i)\sin\alpha$.

In the formula (3.4.16) the second integral coincides with the integral (A.2.9), and third accurate to the angle of a tangent line and replacement of τ_1 with τ_2 coincides at $j = 2$ and $j = N$. We write out the result at $j = N$:

$$
\int\limits_1^{1+\delta} \tilde{R}_{NN}(x)dx = -\delta\frac{\cos\alpha}{r_N}\left[\left(1 + \frac{a}{4}\right)\ln\frac{8r_N}{d} + \frac{a}{4}\right], \qquad \text{(A.2.11)}
$$

where also $d = \delta h$ and $a = (d/r_N)\sin\alpha$.

A.3 Appendix

The equation (3.6.4) differs from the equation (3.1.3) in the summand of the form

$$
\Phi(\xi) = \oint\limits_{L_m} \sigma(\eta(l))\left[\frac{1}{S_m}\oint\limits_{L_m}\frac{\partial G}{\partial n_\xi}(\xi,\zeta(l'))dl'\right]dl\,, \qquad \text{(A.3.1)}
$$

which depends only from the coordinate of the point of observation and, consequently, can be written in the form, similar to (3.2.14):

$$
\Phi_i = \Phi(\xi_i) = \sum_{j=1}^{N_m} H_{ij}\tilde{\sigma}_j\,, \quad i = 1,\ldots,N_m\,, \qquad \text{(A.3.2)}
$$

where $\tilde{\sigma}_j$ accurate to the singularity multipliers coincides with the magnetic charge density in nodes, and H_{ij}) – the regularization correction factor for the matrix F_{ij} (3.2.14).

We calculate at first the integral in square brackets in (A.3.1):

$$A_i = \frac{1}{S_m} \oint\limits_{L_m} \frac{\partial G}{\partial n_{\xi i}}(\xi_i, \zeta) dl' , \qquad i = 1, \ldots, N_m . \tag{A.3.3}$$

When passing from the equation (3.1.3) to (3.2.14) the integral of the following form was calculated:

$$\oint\limits_{L_m} \sigma(\eta) \frac{\partial G}{\partial n_{\xi i}}(\xi_i, \zeta) dl = \sum_{j=1}^{N_m} C^*_{ij} \tilde{\sigma}_j , \qquad i = 1, \ldots, N_m . \tag{A.3.4}$$

It is equal to the integral (A.3.3) at $\sigma(\eta) \equiv 1$ or:

$$a_1(l_j) = a_2(l_j) = \tilde{\sigma}_j = 1 , \qquad j = 1, \ldots, N_m , \tag{A.3.5}$$

where a_1, a_2 – the multipliers of singularities (3.4.12).

Notice, that $a_1(l_j) = a_2(l_j) = 1$, if the singularity powers at each of the segment ends $\tau_1 = \tau_2 = 1$. Calculating the integral (A.3.3) numerically in a similar manner as (A.3.4), one can obtain:

$$A_i = \frac{1}{S_m} \oint\limits_{L_m} \frac{\partial G}{\partial n_{\xi i}}(\xi_i, \zeta) dl' = \frac{1}{S_m} \sum_{j=1}^{N_m} C^{**}_{ij} , \qquad i = 1, \ldots, N_m , \tag{A.3.6}$$

where C^{**}_{ij} is the matrix C^*_{ij}, calculated under conditions (A.3.5). It remains to calculate the integral of the form

$$\oint\limits_{L_m} \sigma(\eta) dl = \sum_{j=1}^{N_m} B_j \tilde{\sigma}_j , \tag{A.3.7}$$

where B_j is the line of the matrix C^*_{ij} (A.3.4) with $\frac{\partial G}{\partial n_{\xi i}}(\xi_i, \eta) \equiv 1$. Then from (A.3.1) and (A.3.2) with regard to (A.3.6) and (A.3.7) we receive the final expression for the matrix regularization factors:

$$H_{ij} = A_i B_j , \qquad (i, j = 1, \ldots, N_m) . \tag{A.3.8}$$

A.4 Appendix

Asymptotics of the functions under the integrals in (4.4.7) has the following form:

$$\begin{aligned} \tilde{G}(\xi, \eta) &= -\ln |(r_0 - r)^2 + (z_0 - z)^2| , \\ \frac{\partial \tilde{G}}{\partial r_0}(\xi, \eta) &= -\frac{2(r_0 - r)}{(r_0 - r)^2 + (z_0 - z)^2} , \\ \frac{\partial \tilde{G}}{\partial z_0}(\xi, \eta) &= -\frac{2(z_0 - z)}{(r_0 - r)^2 + (z_0 - z)^2} . \end{aligned} \tag{A.4.1}$$

We designate $x = z_0 - z$, $y = r_0 - r$. Then the additional integrals in (4.4.7) will be equal to

$$\int\limits_{S_i} \tilde{G}(\xi, \eta) dS = xy \ln(x^2 + y^2) - 3xy + 2x^2 \operatorname{arctg}\frac{y}{x} + (x^2 + y^2) \operatorname{arctg}\frac{x}{y} \Big|_{S_i} ,$$

$$\begin{aligned} \int\limits_{S_i} \frac{\partial \tilde{G}}{\partial r_0}(\xi, \eta) dS &= -x \ln(x^2 + y^2) - 2y \operatorname{arctg}\frac{x}{y} \Big|_{S_i} , \\ \int\limits_{S_i} \frac{\partial \tilde{G}}{\partial z_0}(\xi, \eta) dS &= -y \ln(x^2 + y^2) - 2x \operatorname{arctg}\frac{y}{x} \Big|_{S_i} , \end{aligned} \tag{A.4.2}$$

In the case $r_0 = 0$ the integrals (4.4.5)–(4.4.6) are equal to:

$$\int\limits_{S_i} \tilde{G}(\xi, \eta) dS = \frac{1}{2} \left(x\sqrt{x^2 + y^2} + y^2 \ln |x + \sqrt{x^2 + y^2}| \right) \Big|_{S_i} ,$$

$$\begin{aligned} \int\limits_{S_i} \frac{\partial \tilde{G}}{\partial r_0}(\xi, \eta) dS &= 0 , \\ \int\limits_{S_i} \frac{\partial \tilde{G}}{\partial r_0}(\xi, \eta) dS &= \sqrt{x^2 + y^2} \operatorname{sign}(z_c - z_0) \Big|_{S_i} , \end{aligned} \tag{A.4.3}$$

where z_c is the coordinate of the cell center.

References

[1] *В.Г. Астрелин, В.Я. Иванов.* Пакет программ для расчета характеристик интенсивных пучков релятивистских заряженных частиц. – Автометрия, 1980, №3.

[2] *В.И. Блейвас, В.П. Ильин, В.М. Свешников, В.И. Голубцов, В.П. Самошина, Г.А. Попова.* Комплекс программ для решения на ЭЦВМ "БЭСМ-6" широкого класса задач статической электроники (компилирующая система КСИ-БЭСМ-6), – В сб.: Методы расчета электронно-оптических систем, ч.2. Труды IV Всесоюзного семинара, Новосибирск, 1973.

[3] *В.Я Иванов.* Автоматизация машинного проектирования приборов электроники. – Препринт ВЦ СОАН СССР, 1977, №40.

[4] *R. Mittra, S.W. Lee.* Analytical Techniques in the Theory of Guided Waves, The Macmillian Company, New York, 1971.

[5] *О.В. Тозони.* Метод вторичных источников в электротехнике. М.: Энергия, 1975.

[6] *Y.V. Baryshev et al.* A 100 MW Electron Source with Extremely High Beam Area Compression, NIM-A, vol. A 340, 1994, pp. 241–258.

[7] *Л.Д. Ландау, Е.М. Лифшиц.* Электродинамика сплошных сред. М.: Наука, 1982.

[8] *А.М. Кирьяков, В.А. Попова, Г.А. Шнеерсон.* Расчет напряженности поля вблизи кромки электрода в неоднородной среде. – Известия Академии Наук СССР, Энергетика и Транспорт, 1975, №5.

[9] *D.E. Radley.* The Theory of the Pierce Type Electron Gun, – J. Electron and Control, 1958, №2.

[10] *P.T. Kirstein, G.S. Kino, W.E. Waters.* Space-charge Flow, McGraw Book Co., 1967.

[11] *Д.Д. Рютов.* Об угловых характеристиках электронного пучка, получаемого в бесфольговом диоде. – Препринт ИЯФ 83-146, 1983.

[12] *А.С. Рошаль.* Моделирование заряженных пучков. М.: Атомиздат, 1979.

[13] *K.J. Harker.* Solution of the Cauchy Problem for Laplace's Equation in Axially Symmetric Systems, – J. of Math. Physics, 1963, №7.

[14] *M.M. Karliner at al.* The Magnicon — an Advanced Version of the Gyrocon, NIM-A, vol. A 269, №3, 1988, pp. 459–473.

[15] *И.В. Алямовский.* Электронные пучки и электронные пушки. М.: Советское радио, 1966.

Contents

List of Figures

List of Tables

B.M. Fomel, M.A Tiunov, V.P. Yakovlev

SAM — an Interactive Code for Evaluation of Electron Guns

Б.М. Фомель, М.А. Тиунов, В.П. Яковлев

SAM — интерактивная программа для расчета электронных пушек на мини-ЭВМ

Budker INP 96–11

Ответственный за выпуск С.Г.Попов
Работа поступила 26 октября 1989 г.
Перевод поступил 20 марта 1996 г.

Сдано в набор 21 марта 1996 г.
Подписано в печать 21 марта 1996 г.
Формат бумаги 60×90 1/16 Объем 4,3 печ.л., 3,0 уч.-изд.л.
Тираж 270 экз. Бесплатно. Заказ №11

Обработано на IBM PC и отпечатано на
ротапринте ГНЦ РФ "ИЯФ им. Г.И.Будкера СО РАН",
Новосибирск, 630090, пр. академика Лаврентьева, 11.